JIET

Journal of Investigations on Engineering & Technology

VOLUME: 2 (2019)

ISSUE: 2

ISSN: 2687-3052

Journal of Investigation on Engineering & Technology

http://dergipark.gov.tr/jiet

Product Information
Ürün Bilgisi

Volume *Cilt* **2** **Issue** *Sayı* **2** **December/2019** *Aralık/2019*

Publisher *Yayıncı*	Canan AKSOY
Web Page *Web Sayfası*	http://dergipark.gov.tr/jiet
Date of Publication *Basım Tarihi*	December/2019 *Aralık/2019*
Language *Yayın Dili*	English/Turkish *İngilizce/Türkçe*
Frequency *Yayın Aralığı*	Published twice in a year *Yılda iki kez yayınlanır*
Type of Publication *Yayın Türü*	Periodical *Süreli yayın*
ISSN Number	*2687-3052*

Yazışma Adresi
Karadeniz Teknik Üniversitesi
Teknoloji Fakültesi
İnşaat Mühendisliği Bölümü
Çamlı M. Hacı Mehmet Baheddin Ulusoy
Cad. No:144 61830 Of / TRABZON
Telefon: +90 462 377 84 07
E-posta: jiet@ktu.edu.tr

Correspondence Address
Karadeniz Technical University
Facultu of Technology
Department of Civil Engineering
Çamlı M. Hacı Mehmet Baheddin Ulusoy
St. No:144 61830 Of / TRABZON
Phone: +90 462 377 84 07
E-mail: jiet@ktu.edu.tr

Makale gönderimi dergipark üzerinden yapılmaktadır. Tüm yayınlanan makalelere http://dergipark.gov.tr/jiet adresinden ulaşılabilir.

Paper submission is done via dergipark. All published papers are available at http://dergipark.gov.tr/jiet .

CONTENTS

İçindekiler

Journal of Investigations on Engineering & Technology
Volume 2, Issue 2, 26.12. 2019
ISSN: 2687-3052

Investigation of Rb substitution on the thermoelectric parameters of BSCO Ceramic Materials

B. Özcelik[1], G. Çetin[1], A. Sotelo[2], M.A. Madre[2]

[1]1Department of Physics, Faculty of Sciences and Letters, Çukurova University. 01330 Adana, (Turkey)
[2]ICMA (CSIC-Universidad de Zaragoza). C/Maria de Luna, 3. 50018-Zaragoza (Spain)

(Received: 13.11.2019, Accepted: 17.12.2019, Published Online: 26.12.2019)

Keywords
Thermoelectricoxides;
Resistivity,
Seebeck Coefficient,
Power Factor

Abstract: This study will address the main themes of today, such as reliability, sustainable and clean energy. Within this objective, Bi2Sr2-xRbxCo2Oy materials with x=0.0, 0.025, 0.050, 0.075, 0.100 and 0.125 have been fabricated as powder by solid state technique. From the resistivity graphic, we can reach that pure and 0.025 Rb samples exhibit a semiconducting-like behavior (dρ/dt<0) and the other samples exhibit a metallic-like behavior (dρ/dt>0). The Seebeck coefficients of all samples are determined as positive values for all temperature ranges evidencing the conduction mechanism mainly governed by holes. The maximum power factor values have been obtained in Rb=0.10 sample as 0.19 Mw/K2 at around 650 0C.

1. Introduction

Thermoelectricity (TE) represents the direct solid-state conversion between thermal and electrical energy due to the Seebeck effect. In the current scenario, where more than half of the energy produced end up wasted in form of heat, TE energy conversion constitutes an alternative solution to improve energy efficiency of current industrial and domestic processes. Additionally, TE modules have non-moving parts, which make them silent, reliable and light. TE modules also represent an attractive alternative to power wireless sensors and systems, replacing batteries or expensive wiring. The efficiency of these materials is determined through the figure of merit, ZT (=S2Tσ/κ;S: Seebeck coefficient, T: absolute temperature; σ: electrical conductivity; and κ: thermal conductivity). Consequently, good thermoelectric materials should possess high S, σ, and working T, together with low κ. Nowadays, it is possible to find many works in the literature working on the improvement of ZT mostly by raising their electrical performances [1]. Thermoelectric materials involve a huge family, from semimetals and semiconductors to ceramics obtaining in different crystalline forms, from single crystals and polycrystals to nano-composites [2]. Recently, the best performances were observed in Bi2Te3 [3]. However, it is impossible to use them for the technological applications at high temperatures above room temperature in air-condition. On the other hand after the discovery of NaCoO [4], many experimental studies have been performed in order to find out thermoelectric CoO-based ceramics having a high-performance for using in energy transferred systems [5-8]. The oxide thermoelectric materials can be used at very high temperatures under oxygen media without degradation, due to their good thermal stability. In addition, oxide thermoelectric materials have less toxicity, less costs and relatively low performance comparison to the intermetallic ones. As a result, the main objective of studies has been focused on increasing the thermoelectric performances by using different preparation techniques in CoO-based ceramics via grain orientation [5,9-12], or substitutions [13-16]. The main purpose of this research is to investigate the effect of Rb substitution for Sr in Bi2Sr2Co2Oy system, by measuring the structural and microstructural modifications.

2. Experimental

The Bi2Sr2-xRbxCo2Oy ceramics, (x=0.0, 0.025, 0.050, 0.075, 0.100 and 0.125) were fabricated from

*İlgili yazar: ozcelik@edu.tr ORCID: 0000-0002-8767-1426

commercial powders of Bi2O3, SrCO3, Rb2O, and Co2O3 through the well-know solid state technique. The powders were weighed, mixed, and ball milled at 300 rpm approximately 30 minutes in acetone. The suspension was dried under infrared radiation and manually milled to avoid the agglomerations. The homogeneous suspension was calcined twice: at 750 and 800 °C for 12 h, with an intermediate grinding to degrade the metallic carbonates. Then, the dried powders were uniaxially pressed in form of pellets under an applied pressure of 400 Mpa for 1 minute. Then, these pellets were sintered at 810 ºC for 24h with a final furnace cooling.

Electrical resistivity and Seebeck coefficient were measured with a standard dc four-probe technique in a LSR-3 system in between 50 and 650 ºC under Helyum atmosphere.

3.Results and Discussions

In Fig. 1, as a function of Rb-subtitutions, the variation of electrical resistivity with respect to the temperature is exhibited. As seen in figure, the electrical resistivities of materials are obviously varied by Rb substitution. While pure and x=0.025 samples show semiconducting one ($d\rho/dT<0$), the others exhibit a metallic behaviour ($d\rho/dT>0$). In addition, the values of resistivity slightly reduce up to 0.10Rb, then start to increasing for higher Rb values. This variation can be clarified by the raising of the charge carrier concentration since Rb+ substitution for Sr2+ promotes the oxidation of Co3+ to Co4+ in the conducting layer. In addition, the increasing of electrical resistivity above 0.10Rb may be related to an enhancement of the charge carrier mobility due to the high amount of defects procured by Rubidium substitution. The lowest electrical resistivity value at room temperature is found as 13.7 mΩ.cm in the 0.10Rb sample. This value is lower than the previously announced in materials produced with different methods which is 19-20 mΩ.cm [17,18].

The decreasing of resistivity up to x=0.10Rb content indicates an improvement of electrical conduction arising from Rb substitution. These facts show a lower thermoelectric phase content and a significant increase in the number of grain boundaries in the bulk material. As a result, the charge carriers motion is hampered by these surface detections and reveals a significant electrical resistance.

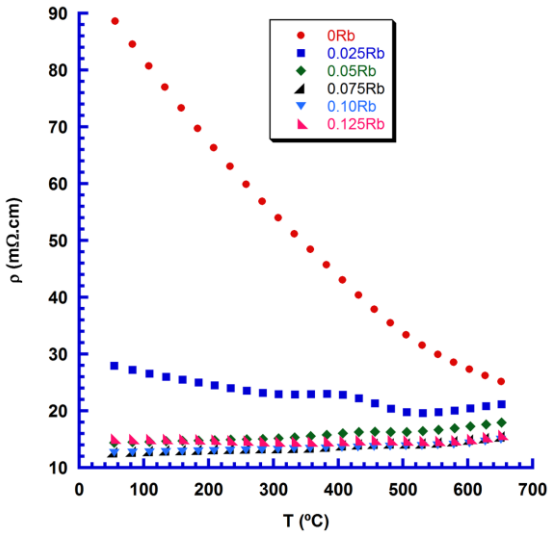

Fig.1. Electrical resistivity versus temperature for Bi2Sr2-xRbxCo2Oy samples

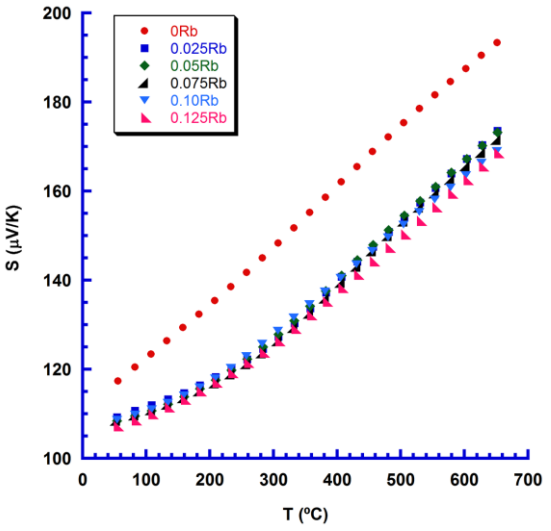

Fig.2. Seebeck coefficient versus temperature for Bi2Sr2-xRbxCo2Oy samples

As a function of Rb-content, in Fig. 2, the change of Seebeck coefficients with respect to temperature are shown. Since the sign of the Seebeck coefficient is always positive in the whole measured temperature range, one can be said that the conduction mechanism in the thermoelectric materials predominantly is controlled by holes. Moreover, for all the samples, the values of Seebeck cooefficient are linearly increased with temperature. This tendecy is

due to a metal or degenerated semiconductor behavior, if the variation of effective mass, Fermi level and carrier concentration with temperature are negligible. Moreover, all Rb-substituted samples have lower Seebeck coefficient comparison to the pure sample which is in agreement with the resistivity results.

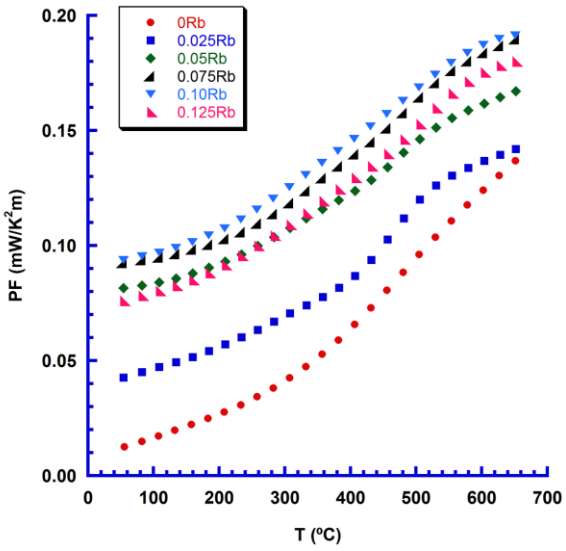

Fig.3. Power factor versus temperature for Bi2Sr2-xRbxCo2Oy samples

From the resistivity and Seebeck data, the thermoelectric performances of samples, known as power factor (PF), as a function of temperature were calculated by using PF= S2/ρ formula. The results are presented in Fig. 3. As can be observed that all Rb substituted materials have higher power factor values comparison to the pure sample resulting of the drastic decrease in the electrical resistivity caused by Rb. The maximum value at room temperature is found as 0.095 mW/K2m for 0.10Rb substituted material which is higher than the previously reported studies [17,18].

4. Conclusions

In this study, Bi2Sr2-xRbxCo2Oy samples (x = 0, 0.025, 0.05, 0.075, 0.10, and 0.125) have been produced via the solid-state technique. A drastic decline in resistivity comparison to the pure sample has been found in Rb substituted materials due to the increment of their density. No significant variation of Seebeck coefficient was observed, causing of higher PF values in all the Rb substituted materials. For x=0.10Rb, the maximum PF value was calculated as 0.192 mW/K2.m at 650 ºC. This clearly indicates that Rb inclusion is a feasible technique in order to obtain the thermoelectric ceramic materials having high performances.

Acknowledgement: This work is supported by Research Fund of Çukurova University, Adana, Turkey, under grant contracts no: FBA-2019-12034.

References

[1] D. M. Rowe, Thermoelectrics Handbook: Macro to Nano, 1st edn. CRC Press, Boca Raton, (2006).

[2] J.-C. Zheng, Recent advances on thermoelectric materials, Front. Phys. China 3, 269–279 (2008).

[3] H. C. Wang, J.-H. Bahk, C. Kang, J. Hwang, K. Kim, J. Kim, P. Burke, J. E. Bowers, A. C. Gossard, A. Shakouri, W. Kim, Right sizes of nano- and microstructures for high-performance and rigid bulk thermoelectrics, P. Natl. Acad. Sci. USA 111, 10949-10954 (2014).

[4] I. Terasaki, Y. Sasago, K. Uchinokura, Large thermoelectric power in NaCo2O4 single crystals, Phys Rev B. 56, 12685-12687 (1997).

[5] N. M. Ferreira, Sh. Rasekh, F. M. Costa, M. A. Madre, A. Sotelo, J. C. Diez, M. A. Torres, New method to improve the grain alignment and performance of thermoelectric ceramics, Mater. Lett. 83, 144–147 (2012).

[6] Y. H. Zhu, W. B. Su, J. Liu, Y. C. Zhou, J. Li, X. Zhang, Y. Du, C. L. Wang, Effects of Dy and Yb co-doping on thermoelectric properties of CaMnO3 ceramics, Ceram. Int. 41, 1535-1539 (2015).

[7] J. Liu, C. L. Wang, Y. Li, W. B. Su, Y. H. Zhu, J. C. Li, L. M. Mei, Influence of rare earth doping on thermoelectric properties of SrTiO3 ceramics, J. Appl. Phys. 114, 223714 (2013).

[8] J. G. Noudem, S. Lemonnier, M. Prevel, E. S. Reddy, E. Guilmeau, C. Goupil, Thermoelectric ceramics for generators, J. Eur. Ceram. Soc. 28, 41–48 (2008).

[9] H. Itahara, C. Xia, J. Sugiyama, T. Tani, Fabrication of textured thermoelectric layered cobaltites with various rock salt-type layers by using b-Co(OH)2 platelets as reactive templates, J. Mater. Chem. 14, 61–66 (2004).

[10] H. Wang, X. Sun, X. Yan, D. Huo, X. Li, J.-G. Li, X. Ding, Fabrication and thermoelectric properties of highly textured Ca9Co12O28 ceramic, J. Alloys Compds. 582, 294-298 (2014).

[11] S. Butt, J.-L. Liu, K. Shehzad, B. Zhan, Y. Lin, C.-W. Nan, High-temperature thermoelectric properties of La and Fe co-doped Ca–Co–O misfit-layered cobaltites consolidated by spark plasma sintering, J. Alloys Compds. 588, 277-283 (2014).

[12] A. Sotelo, Sh. Rasekh, G. Constantinescu, M. A. Torres, M. A. Madre, J. C. Diez, Improvement of textured Bi1.6Pb0.4Sr2Co1.8Ox thermoelectric performances by metallic Ag additions, Ceram. Int. 39, 1597-1602 (2013).

[13] N. Sun, S. T. Dong, B. B. Zhang, Y. B. Chen, J. Zhou, S. T. Zhang, Z. B. Gu, S. H. Yao, Y. F. Chen, Intrinsically modified thermoelectric performance of alkaline-earth isovalently substituted [Bi2AE2O4][CoO2]y single crystals, J. Appl. Phys. 114, 043705 (2013).

[14] Sh. Rasekh, M. A. Madre, J. C. Diez, E. Guilmeau, S. Marinel, A. Sotelo, Effect of Pb substitution on the thermoelectrical properties of textured Bi2Ca2Co1.7Oy ceramics prepared by a polymer solution method, Bol. Soc. Esp. Ceram. Vidr. 49, 371-376 (2010).

[15] G. Constantinescu, Sh. Rasekh, M. A. Torres, J. C. Diez, M. A. Madre, A. Sotelo, Effect of Sr substitution for Ca on the Ca3Co4O9 thermoelectric properties. J. Alloys Compds. 577, 511-515 (2013).

[16] S. Pinitsoontorn, N. Lerssongkram, N. Keawprak, V. Amornkitbamrung, Thermoelectric properties of transition metals-doped $Ca_3Co_{3.8}M_{0.2}O_{9+\delta}$ (M = Co, Cr, Fe, Ni, Cu and Zn), J. Mater. Sci.: Mater. Electron. 23, 1050-1056 (2012).

[17] M. A. Torres, A. Sotelo, Sh. Rasekh, I. Serrano, G. Constantinescu, M. A. Madre, J. C. Diez, Improvement of thermoelectric properties of Bi2Sr2Co1.8Ox through solution synthetic methods, Bol. Soc. Esp. Ceram. V. 51, 1-6 (2012).

[18] E. Combe, R. Funahashi, F. Azough, R. Freer, Relationship between microstructure and thermoelectric properties of Bi2Sr2Co2Ox bulk materials, J. Mater. Res. 29, 1376-1382 (2014).

Journal of Investigations on Engineering & Technology
Volume 2, Issue 2, 26.12. 2019
ISSN: 2687-3052

Determination of the intrinsic viscosity and molecular weight of Poly(methyl methacrylate) blends

Y. Yigit[1], A. Kilislioglu[2], S. Karakus[2], N. Baydogan[1]*

[1]Istanbul Technical University, Energy Institute, Ayazaga Campus, Maslak, 34469, Istanbul, Turkey
[2]Istanbul University-Cerrahpasa, Department of Chemistry, Faculty of Engineering, Avcilar, 34320 Istanbul, Turkey

(Received: 18 .11.2019, Accepted: 17.12.2019, Published Online: 26.12.2019)

Keywords
Poly(methyl methacrylate)
Viscosity
Average Molecular Weight

Abstract: PMMA blends were synthesized through Atom Transfer Radical Polymerization (ATRP) method under at different concentration ratios. The viscosity characteristics of the structure were investigated to determine the behavior of macromolecules in blends. The viscosity characterization of the nanoparticles was determined to explain the molecular structure and interactions. The intrinsic viscosity of the blend was calculated with three different models including Huggins, Kraemer, and Rao. All blends were performed to understand the effect of additives concentration on molecular conformations and the intrinsic viscosity of the polymers. The voluminosity (V_E) and the shape factor (υ) were calculated for the blends to understand the miscibility behavior. From experimental results, it was observed that the intrinsic viscosity was increased with the increase in the amount of substance and the solubility of the system in solution.

1. Introduction

The controlled /living radical polymerization is a radical polymerization that can be stopped and re-initiated under external control. There are three types methods used for the controlled /living radical polymerization and they are applied to a large number of monomers. The applied methods are nitroxide mediated polymerization (NMP), metal-catalyzed atom transfer radical polymerization (ATRP), and reversible addition-fragmentation chain transfer (RAFT) [1]. The chain transfer and the termination reactions can be eliminated in controlled radical polymerization. The molecular weight and polydispersibility are adjustable to produce polymers without being affected by chain transfer processes. The use of the living radical polymerization presents some advances in compare to conventional free radical polymerization. The main advantages of the living polymerization are predetermined molar mass and control over end-groups. Besides, the use of ATRP technique has several advantages: catalytic amounts of transition metal complexes are used; many initiators are commercially available, including multifunctional and hybridsystems; a large range of monomers can bepolymerized (with the exception of unprotectedacids); end-functionalization is very simple; a large range of temperatures can be employed [2].

1.1 Molecular weight

Poly (methyl methacrylate) (PMMA) recognized as plexiglass or acrylic glass [3]. The trade names of PMMA are plexiglas, acrylite and lucite. PMMA has the transparent and thermoplastic properties and generally utilized in sheet form [4]. It is a lightweight choice among the glassy materials [5]. Whereas molecules or atoms in crystalline materials are linked to one another in a certain order polymer materials which can be formed by more than one chain have a random sequence. Polymer materials consist of chains, and these chains may vary in number in terms of the monomer which is the building block of polymers. Therefore, it is not possible to mention a single molecular weight in most of polymer materials. [6-7].

There are 4 kinds of molecular weight in polymers:

a) Number Average Molecular Weight (M_n) which can be expressed briefly in Eq-1: it is obtained by dividing the total molecular weight by the total number of molecules. It is obtained by methods based on the measurement of colligative properties such as freezing point descent, boiling point rise, osmotic pressure, vapor pressure drop.

$$M_n = \frac{\sum_i N_i M_i}{\sum_i N_i} \quad (1)$$

*Corresponding author: doganni@itu.edu.tr ORCID: 0000-0001-9843-1615

b) Weight Average Molecular Weight (Mw), the higher the molecular weight of the molecule, the greater the effect of the molecule on the Weight Average Molecular Weight of the polymer. Unlike first kind of molecular weight molecules forming polymers do not have the same effect in calculating of molecular weight. It can be calculated in Eq-2:

$$M_w = \frac{\sum_i N_i M_i^2}{\sum_i N_i M_i} \quad (2)$$

where M_i is the molecular weight of a chain, N_i is the number of chains of that molecular weight, and i is the number of polymer molecules [8].

c) Z-Average Molecular Weight (M_z), it is an uncommon type of molecular weight .It is obtained by ultracentrifugation method. It is used to determine mechanical properties such as toughness. It can be calculated in Eq-3:

$$M_z = \frac{\sum_i N_i M_i^3}{\sum_i N_i M_i^2} \quad (3)$$

where M_i is the molecular weight of a chain, N_i is the number of chains of that molecular weight, and i is the number of polymer molecules [9].

d) Viscosity Average Molecular Weight (M_v), Viscosity is the measure of resistance to flow and the viscosity of the solid materials is calculated by dissolving in a suitable solvent. M_v is briefly calculated in this way: the polymer material is diluted in a suitable solvent in different proportions. So, solutions are obtained at different concentrations. The viscosities of these diluted solutions are calculated, and then the molecular weight of the polymer material is calculated. The relationship between viscosity and molecular weight can be explained as follows. Flowing of large chain polymers is difficult due to entanglement and friction between the chains. That makes the solution ticker and these exhibit higher viscosities.

The intrinsic viscosity, η as function of average molecular weight, M is represented by Mark-Houwink Sakurada equation (in Eq-4).

$$[\eta] = KM^{\alpha} \quad (4)$$

: where K and α are empirically determined constants for a given polymer solvent temperature system.
As it can be seen in equation 1-2-3, the distribution of molecular weights in a heterogeneous polymer is that $M_z > M_w > M_v > M_n$. This can be easily applied in Figure 1 [10].

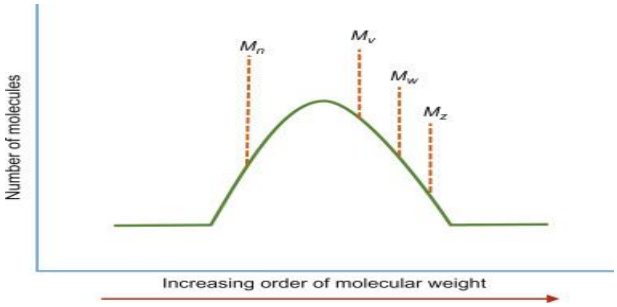

Figure 1. Demonstration of molecular weights in a heterogeneous polymer [10].

1.2 Polydispersity

Monodisperse (some natural polymer) molecular weights of all polymer molecules are same. Polydisperse pronounces for synthetic polymers and the distributed molecules and it is named as Polydispersity Index (PI). It is a measure of heterogeneity within the structure. If PI is 1, then $M_w=M_n$ like some natural polymers molecular weight is identical in all structure. If PI is more than 1, $M_n>M_w$ and there is heterogeneity within the structure.

One of the most desirable properties of materials used in engineering is the homogeneous structure. As the polydispersity increases, heterogeneity in the structure will increase, and especially mechanical differences will occur within the structure. It must be reduced the heterogeneity of the structure to eliminate these unwanted mechanical differences. In recent years, polymers have been started to produce between 1.0 and 1.2 PI and this rate of heterogeneity has been gradually reduced as molecular weight differences in the structure are requested to be reduced to the minimum level (Figure 2) [11].

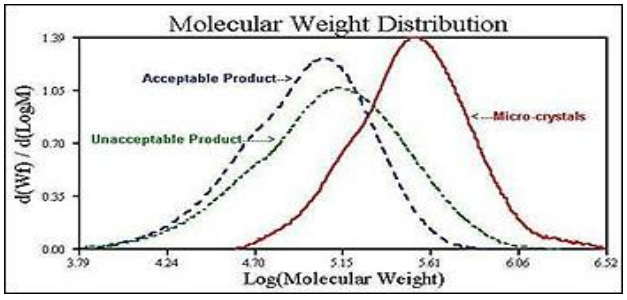

Figure 2. Molecular Weight Distribution [11].

1.3 Relationship between viscosity and mechanical properties

High mechanical values are desirable, however it is observed that it crawl after an approximate value of

molecular weight whereas the viscosity exhibits a continuous increase with increasing molecular weight [12-17]. Since the high viscosity means difficult molding of the material, an optimization is needed between these values. This value of molecular weight is 10000-1000000 g/mol. The above mentioned information is clearly seen in the Figure 3 [12].

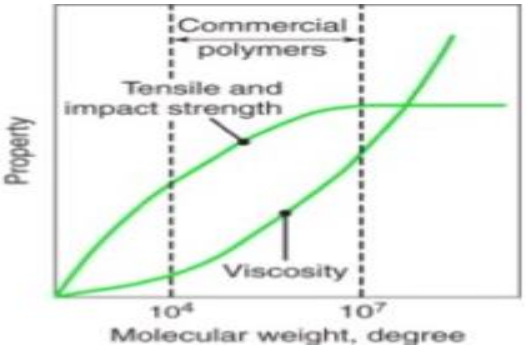

Figure 3. Relationship between viscosity and mechanical properties [12].

2. Experiments

The used chemicals for the synthesis of PMMA produced by ATRP method:

- MMA($C_5H_8O_2$)=50 mL, d=0.939 g/cm^3, 0.4695 mol
- EBİB($C_6H_{11}BrO_2$) =0.7826 mmol (density=1.329 g/cm^3, Vebib= 115.987µL)
- PMDETA($C_9H_{23}N_3$)=0.0004 mol (denstiy =0.830 g/cm^3,Vpmdata=164.290 µL)
- Bu_4NBr=2.00920 g
- CuBr=0.11176 g

Bu_4NBr (Tetra-n-butylammonium Bromide) was used as solvent at the production of PMMA. Bu_4NBr concentration was increased double amount in PMMA solution to evaluate the molecular weight variations of PMMA by using the maximum amount of the solvent in PMMA solution.

2.1 Measurement of Viscosity for the Determination of Average Molecular Weight

Viscosity average molecular weight test belonging base PMMA by ATRP was performed in the following order to obtain homogeneous solution

Weighing of Polymer Samples by using Sensitive Balance to be Measured Viscosity: The samples (0.1g, 0.3 g, 0.5 g and 0.8 g) belonging base PMMA by ATRP was weighed respectively on the precision scale, whose brand is Radwag AS 220 / C / 2 and whose accuracy is 10^{-4} g .

Preparation of Solvent: 50 mL of toluene was used as solvent in each sample and the used toluene was measured in the measuring cylinder. Solution Preparation and Measures Taken to Maintain the Amount of Solvent: Measured toluene, PMMAs and magnetic stir bar making the mixture homogeneous are placed in the conical flask. Since toluene is a volatile material, this flask was sealed to be airtight. Any loss in toluene results in a difference between the target concentration and the concentration obtained. This also leads to erroneous results.

The flask was placed on a magnetic stirrer set at 250 revolutions per minute at room temperature to obtain homogeneous solution.

Measuring the Viscosity of the Solution: When the solutions became homogeneous, the flasks were taken from the magnetic stirrer and the viscosities of the mixtures were measured by means of a viscometer. The measurements were carried out with AND-SV-10 viscometer. This viscometer has anaccuracy with 0.01 cP for the measurements.

When the solutions became homogeneous, the flasks were taken from the magnetic stirrer and the viscosities of the mixtures were measured by means of a viscometer. The measurements were carried out with AND-SV-10 viscometer. This viscometer is able to measure with accuracy of 0.01 cP.

Table 1. Equation constants for various polymer-solvent pairs [17].

Polymer-solvent system	K x 10^3 mL/g	α (Equation constant)
PMMA-Acetone	7.70	0.700
PMMA-Benzene	5.20	0.760
PMMA-Toluene	***7.00***	***0.710***
Poly vinyl acetate-Acetone	10.20	0.720
Poly vinyl acetate-Benzene	56.30	0.620
Poly vinyl acetate-Acetonitrile	41.50	0.620
Poly vinyl alcohol-Water	45.30	0.640
Poly styrene-Benzene	10.60	0.735
Poly styrene-Toluene	11.00	0.725

Equations and expressions used to measure the viscosity molecular weight of solution: the results were used to obtain relative viscosity and specific viscosity, reduced viscosity, inherent viscosity, intrinsic viscosity. Finally, calculated intrinsic viscosity used in the Mark-Houwink equation. Where η (the intrinsic viscosity), M (Molecular weight) and α, K constants for the particular polymer solvent system. The appropriate solvent for the produce PMMA in this study was toluene and its fixed value was presented in Table 1. The result with viscosimetric molecular weight test was determined and Mark-Houwink equation (Eq-4). η was

determined ascut-off point of y axes, k was constant for toluene (0.007 mL/g), α was constant for toluen (0.71) as solvent, M=Avarage Molecular Weight (in Eq-4).

The molecular weight of the polymer was measured by using viscometer and the molecular weight called viscosity average molecular weight obtained by this technique. The mechanical properties of the polymers which are anisotropic materials can be modified according to the directions, as PMMA molecular weight is livingpolymer. The molecular weight and chain uniformity of the structure will be determined according to $[\eta] = KM^{\alpha}$ (in Eq-4). $[\eta]$: intrinsic viscosity, M: molecular weight, K and α are empirically determined constants for a given polymer solvent temperature system. After intrinsic viscosity value was determined by viscometer method, molecular weight was determined [13]. Assessment of intrinsic viscosity [η] was evaluated. For this purpose, the relative viscosity (η_{rel}) (Eq-5) was calculated from the ratio between the flow time of the polymer solution (t) and the flow time of the pure solvent (t_0). Relative viscosity (η_{sp}), [η] and inherent viscosity (η_{inh}) were determined by using Eq. 5-8 [12-14].

Relative viscosity:

$$\eta_{rel} = \frac{t}{t_0} \quad (5)$$

Specificviscosity:

$$\eta_{sp} = \frac{t}{t_0} - 1 = \eta_{rel} - 1 \quad (6)$$

Intrinsic viscosity:

$$[\eta] = \frac{t - t_0}{t_0 * C} = \frac{\eta_{sp}}{C} \quad (7)$$

Inherent viscosity:

$$\eta_{inh} = In\frac{t/t_0}{C} = In\frac{\eta_{rel}}{C} \quad (8)$$

3. Results

Table 2 presents the values to determine the viscosity of the solvent and the solutions at different concentrations. Table 3 shows the viscosities of the solutions at different concentrations used to calculate the instristic viscosity value.

Table 2. Information about base PMMA.

Amount of PMMA (g)	Solvent (Touluen) Amount (ml)	Concentration of Solution (g/ml)	Solvent Touluen Viscosity (cP)	Solution Viscosity (cP)
0.1	50	0.002	0.58	0.64
0.3	50	0.006	0.58	0.68
0.5	50	0.01	0.58	0.78
0.8	50	0.016	0.58	0.88

Table 3. Changes in the inherent viscosity of the solutions at different concentrations for base PMMA.

Relative Viscosity (η_r)	Specific Viscosity (η_{sp})	Reduced Viscosity (η_{red})	Inherent Viscosity (η_{inh})
1.103448276	0.103448276	51.72413793	49.22003641
1.172413793	0.172413793	28.73563218	26.51078244
1.344827586	0.344827586	34.48275862	29.62658161
1.517241379	0.517241379	32.32758621	26.05586275

The assessment of intrinsic viscosity for base PMMA was presented in Figure 4. Hence, average molecular weight is determined by using Eq-4. A result of the calculations, the average molecular weight of base PMMA was found to be 274.042 g / mol.

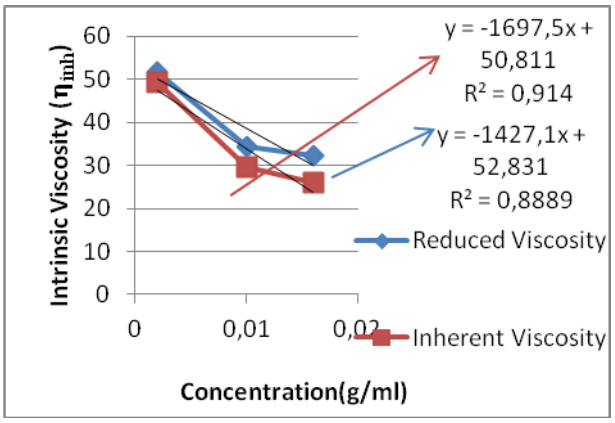

Figure 4. The assessment of intrinsic viscosity of base PMMA.

4. Discussions

Synthetic polymers do not consist of the same chains as crystalline atoms or molecules and in them cannot be mentioned a constant molecular weight [16-19]. In addition to that, the obtained molecular weight values can be influenced by many parameters of production [20-22]. The molecular weight values of polymer materials are available in a range for several materials in Table 4 [18].

Table 4. Molecular Weight of Various Molecules [18].

Molecules	Molecular weight (g/mol)
Water	18
Alcohol	46
Stearic Acid	384
Polistiren	60.000-100.000
Low Density Polyethylene (LDPE)	30.000-60.000
High Density Polyethylene (HDPE)	30.000-150.000

PMMA synthesized by using different techniques has an average molecular weight in the range of 42.000-130.000. Since, the increase of the value in a controlled manner means improvement of mechanical properties, the average molecular weight was increased by several methods (such as, ATRP, ARGET ATRP). The effect of ATP on molecular weight was clearly examined in Table 5. The average molecular weight of the base PMMA was determined as ~ 270.000 g/mol. The results indicate that the molecular weight has higher than that of industrial PMMAs.

Table 5. Average Molecular Weight of base PMMA.

Material	Avarage Molecular Weight (g/mol)
PMMA [17] (by GPC)	120.000
PMMA [18] (PMMA prepared from the block copolymer micelle/homopolymer)	90.000
PMMA [19] (PMMA synthesed by the catalyzed recyclable Ni–Co alloy nanoparticle)	129.500 (Mw/Mn=1,300)
PMMA [20] (ARGET ATRP)	42.500 (PDI=1.36)
PMMA (produced by ATRP method in this study)	274.043

PDI: Polydispersity index.

GPC: A gel permeation chromatography.

ARGET: Activators regenerated by electron transfer.

5. Conclusions

The results of this study indicated that PMMA produced by ATRP method was suitable technique to improve the average molecular weight in this study. PMMA produced by ATRP method named the living polymerization technique has higher the average molecular weight than the molecular weight of the PMMA produced by different techniques in the literature. The molecular weight for the PMMA produced by ATRP method was determined ~270.000 g/mol.

Acknowledge

This work was supported financially by Istanbul Technical University Scientific Research Projects Foundation, ITU BAP, MSc. Thesis Project with MGA-2018-41576 project number.

References

[1] K. Matyjaszewski. Comparison and Classification of Controlled/Living Radical Polymerizations, Chapter1, ACS Symposium Series, Vol. 768 (2000), DOI: 10.1021/bk-2000-0768.ch001.

[2] Braunecker W. A., Matyjaszewski K., Controlled/living radical polymerization: Features, developments, and perspectives, Prog. Polym. Sci. 32 (2007) 93–146.

[3] T. Bel, C. Arslan, N. Baydogan, Materials Chemistry and Physics, 221, p. 58-67 (2019).

[4] T. Bel, C. Arslan, N. Baydogan, Journal of the Faculty of Engineering and Architecture of Gazi University, 2018, 18-1 DOI: https://doi.or./ p. 1-18, (2018).

[5] T. Bel , H. Cakar , N. Yahya , C. Arslan , N. Baydogan, Defect and Diffusion Forum, 380, p. 227-231, (2017).

[6] A. Rudin, Mechanical properties of polymer solids and liquids, in: A. Rudin (Ed.), Elements of Polymer Science and Engineering, second ed., Academic Press, San Diego, 1999, pp. 377_443.

[7] M. Chanda, Introduction to Polymer Science and Chemistry: A Problem-Solving Approach, second ed., CRC Press, Boca Raton, FL, 2013, p. 29.

[8] L.W. McKeen, Permeability Properties of Plastics and Elastomers, third ed., William Andrew Publishing, Oxford, 2012, pp. 21_37.

[9] J.L. Schultz, E.S. Wilks, Nomenclature of Polymers, Encyclopedia of Polymer Science and Technology, Wiley, Hoboken, NJ, 2000.

[10] The Effect of Creep and Other Time Related Factors on Plastics and Elastomers (Second Edition), 2009

[11] https://www.laboratorynetwork.com/doc/analysis-method-ensures-better-polymer-qualit-0001

[12] https://www.chegg.com/homework-help/questions-and-answers/define-molecular-weight-degree-polymerization-graphical-relationship-molecular-weight-poly-q12052059

[13] Chuah, H. H., Lin-Vien, D., &Soni, U. (2001). Poly (trimethylene terephthalate) molecular weight and Mark–Houwink equation. Polymer, 42(16), 7137-7139.

[14] F. Behrouzian, S. M. Razavi, H. Karazhiyan, Intrinsic viscosity of cress (Lepidiumsativum) seed gum: effect of salts and sugars. Food Hydrocolloid. 35 (2014) 100-105.

[15] S. M. Razavi, T. M. Moghaddam, B. Emadzadeh, F. Salehi, Dilute solution properties of wild sage (Salvia macrosiphon) seed gum. Food Hydrocoll. 29(1) (2012) 205-210.

[16] R. Pamies, J. G. H. Cifre, M. D. C. L. Martínez, J. G. de la Torre, Determination of intrinsic viscosities of macromolecules and nanoparticles. Comparison of single-point and dilution procedures, Colloid Polym. Sci. 286(11) (2008) 1223-1231.

[17] https://vlab.amrita.edu/?sub=2&brch=190&sim=603&cnt=1

[18] https://www.sciencedirect.com/science/article/pii/0032386177900891?via%3Dihub

[19] https://www.sigmaaldrich.com/catalog/product/aldrich/182230?lang=en&region=TR

[20] Hyungmin Park, High-throughput preparation of complex multi-scale patterns from block copolymer/homopolymerblend films.

[21] SkArif Mohammad, Recoverable and recyclable nickel–cobalt magnetic alloy nanoparticle catalyzed reversible deactivation radical polymerization of methyl methacrylate at 25 °C

[22] Hyun Jeong Jeon, Synthesis of high molecular weight 3-arm star PMMA by ARGET ATRP

Journal of Investigations on Engineering & Technology
Volume 2, Issue 2, 26.12. 2019
ISSN: 2687-3052

The Effect of Calcination Conditions on Luminescence Efficiency of BeO Ceramics Synthesized Using Co-Precipitation Method

Volkan ALTUNAL*[1], Veysi GÜÇKAN[1], Adnan ÖZDEMİR[1], Zehra YEĞİNGİL[1]

[1]Çukurova University, Art and Science Faculty, Physics Department, 01330, Adana

(Received: 23.10.2019, Accepted: 23.12.2019, Published Online: 26.12.2019)

Keywords
Beryllium oxide (BeO)
Calcination Conditions
Radiation Dosimetry

Abstract: BeO ceramics were synthesized by co-precipitation method. The luminescent behaviors of the BeO ceramics prepared under different reaction conditions were investigated for radiation dosimetry applications. The appropriate calcination temperature and time for the sol-gel synthesis of BeO were determined as 1000 °C for 4 hours by analyzing optically stimulated luminescence (OSL), thermoluminescence (TL) sensitivities and radioluminescence (RL) emissions of the products. While similar characteristic broad emission peak of BeO ceramics between 200 and 500 nm was obtained in RL spectra, an unexpected peak between 650 and 800 nm which may be associated with the anion defects in BeO was observed. While highly sensitive two TL peaks were observed up to 250 °C, low sensitive four TL peaks were found up to 650 °C. The results showed that luminescent signals from the BeO pellets produced at appropriate synthesis conditions were suitable for radiation measurement applications in personal dosimetry.

1. Introduction

New and rapidly developing applications in physics and medicine encourage researchers to produce new materials. The synthesis process is very important as it affects the general properties of the produced materials. Moreover, the ceramic preparation process has to incorporate a variety of production techniques (for micro and nanostructures). Micro or nanostructures, synthesis conditions (calcination and sintering) and particle size change the luminescence properties of ceramics [1]. Another factor affecting the luminescence properties of ceramics is the synthesis method. For example, narrow particle size distribution and high homogeneity are provided in the sol-gel method, while low cost, controllable and small particle size in the precipitation method provides an easy synthesis process. Luminescent emitting ceramics are used in many areas such as lighting, display, radiation dosimeters [2, 3]. Specifically, the use of ceramic materials in radiation dosimetry is increasing day by day with the discovery of materials (Al_2O_3, BeO, MgO, etc.) having unique physical, chemical, and luminescence properties. BeO Thermalox995 chip (from Materion Corporation), together with Al_2O_3:C (Al_2O_3:C from Landauer Inc.) nano-Dot dosimeter, is one of the ceramic materials commonly used in OSL dosimetry. It has been known for over 50 years that the material exhibits TL and OSL signals [4-8]. Being a tissue-equivalent material (Z_{eff} ~7.1) [9], not losing radiation dose for about 6 months [10], thermal stability and light sensitive dosimeter attracted researchers [8], and recently produced BeO-based OSL dosimetry system as a product of ongoing studies [10-12].

In this study, BeO ceramics were synthesized using the precipitation method. To obtain more stable luminescent signals from the surface of ceramics, BeO samples were prepared in pellet form from the nano-powders. The effects of calcination temperature and duration on luminescence signals were investigated using TL, OSL, and RL techniques. We investigated whether the usage of appropriate calcination conditions in BeO precipitation synthesis is a good starting operation to achieve a promising OSL dosimeter with high luminescent efficiency, or not.

2. Material and Method

All reagents, polyethyleneimine solution (Analytical standard, 50 % (w/v) in H_2O), ammonium hydroxide solution (NH_4OH) (ACS reagent, 28.0-30.0% NH3 basis) and beryllium sulfate tetra-hydrate ($BeSO_4 \cdot 4H_2O$) (99.99% trace metals basis) with high purity used in synthesis were purchased from Sigma

*Corresponding author: valtunal@cu.edu.tr ORCID: 0000-0001-9411-3441

Aldrich. The synthesis process began with the complete dissolution of beryllium sulfate salts in distilled water. On the other hand, the polyethyleneimine solution was stirred in distilled water for a certain period of time and added to the main solution slowly. Thus, the precipitation process started. The pH control of the solution was carried out by adding a certain amount of ammonia to the main solution. During the ongoing stirring, the precipitate was observed and the solution in the beaker was transferred to a suitable crucible. Then the temperature of the main solution in the crucible was increased to 200 °C, and the water in the solution was removed. The calcination process was carried out to remove the organics from the final product and to obtain the form of pure BeO. In this study, while the calcination temperatures were selected as 800, 900, 1000, 1100 and 1200 °C, the duration times were 2, 4, 6, 8, 10 and 24 hours. After the calcination process, BeO samples were prepared in pellet form by using pure BeO powders for easy handling and to obtain stable luminescent signals from the surfaces of BeO. Here, the applied pressure was 500 kg force/cm^2 and duration time was 1 min. Finally, to correct trap structures and achieve a uniform crystal structure, prepared pellets were sintered at 1600 °C, for 4 h. The photo of the BeO ceramics synthesized by precipitation method was shown in Fig. 1.

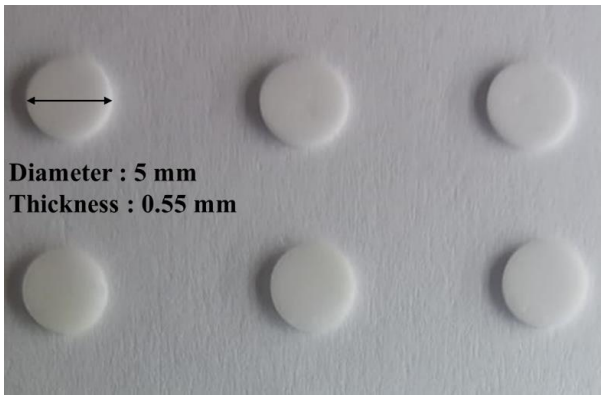

Figure 1. The produced BeO pellets

After the sample preparation, TL and OSL measurements were performed using the DA-20 model RisØ TL/OSL reader system equipped with a ^{90}Sr-^{90}Y beta radiation source with the energy of 2.27 MeV and bialkali model 9235 QA photomultiplier tube. Light stimulations were used in continuous wave OSL mode by blue LEDs (λ ~ 470 nm). TL and OSL signals were detected using a Hoya U-340 nm UV pass filter in front of PMT. RL emissions of the BeO pellets were obtained from a homemade X-ray Luminescence system equipped with a 4-40 kV X-ray tube and USB-2000 model Ocean Optics fiber spectrometer which is produced for low sensitivity applications.

3. Results and Discussion

3.1. RL Emissions

RL emissions were obtained from the BeO pellets calcinated at a different calcination temperature of 800, 900, 1000, 1100 and 1200 °C for 4 h in Fig. 2. According to RL emissions, since the maximum intensity was obtained from the BeO pellets calcinated at 900 °C, the appropriate calcination temperature was selected as 900 °C. After the determination of the appropriate calcination temperature, BeO materials were synthesized in a similar way and calcinated at 900 °C for different calcination duration of 2, 4, 6, 8, 10, and 24 hours. RL emissions for different durations were presented in Fig. 3. According to RL emissions in Fig. 3., the maximum intensity was obtained from the BeO pellets calcinated at 900 °C for 4 h. The appropriate calcination duration was selected as 4 h.

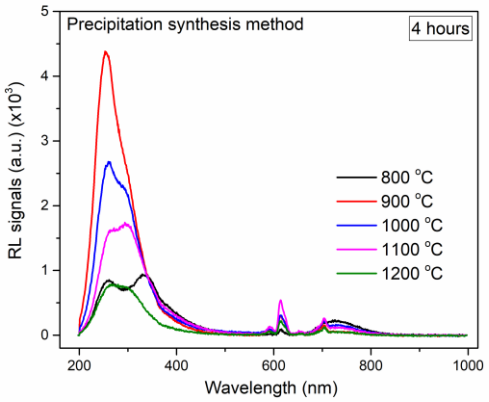

Figure 2. RL emissions of BeO pellets which were calcinated at different temperatures for 4 h.

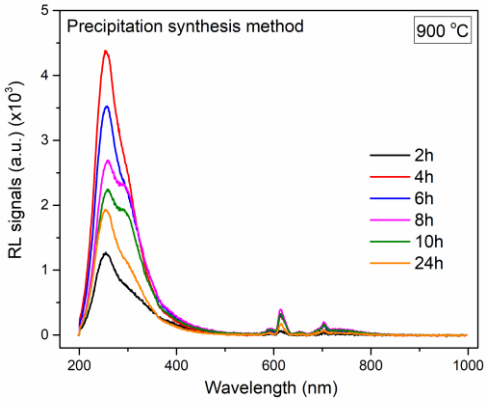

Figure 3. RL emissions of BeO pellets which were calcinated at 900 °C for different durations.

On the other hand, all the obtained RL emissions show the same broad highly sensitive emission peak located between 200 and 500 nm. This characteristic luminescence emission (3-4 eV and 4.9 eV) is

associated with the radiative annihilation of the self-trapped excitons in BeO [13, 14]. Additionally, the emission peaks located at 590, 620 and 640 nm are originated from the background signals of the RL system. Unexpected emissions located between 700 and 800 nm is associated with the oxygen defects in BeO may act as anion defects in the structure. It is known that such anion defects occurring during synthesis in the structure may show large emissions at high wavelengths in RL measurements.

3.2. TL Glow Curves

Fig. 4. shows TL glow curves obtained from the BeO pellets calcinated at a different calcination temperature of 800, 900, 1000, 1100 and 1200 °C for 4 h. As seen from Fig 4., BeO pellets exhibited three TL peaks located at 170, 260 and 440 °C. Similar TL trap distribution was presented by Altunal et al. [13]. Due to maximum intensity at 900 °C, the appropriate calcination temperature was selected as 900 °C. After the determination of the appropriate calcination temperature, BeO materials were synthesized in a similar way and calcinated at 900 °C for different calcination duration of 2, 4, 6, 8, 10, and 24 hours. TL glow curves for different durations were presented in Fig. 5. Finally, the maximum trapped charge population was obtained from the BeO pellets calcinated at 900 °C for 4 h. Considering all the TL glow curves of BeO samples, the total charge population gave the maximum value for the sample calcined at 900 °C for 4 h because different calcination conditions do not change the structure of TL traps in BeO.

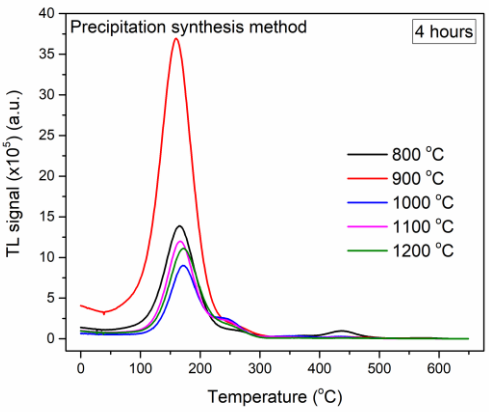

Figure 4. TL glow curves of BeO pellets calcinated at different temperatures for 4 h.

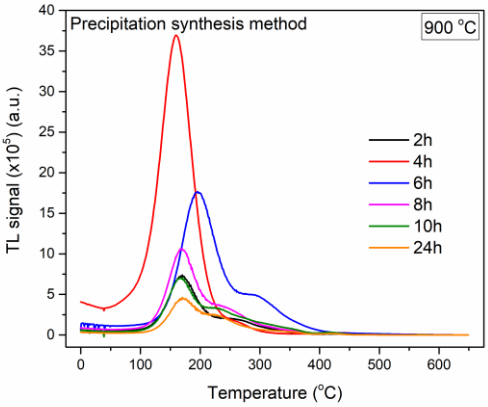

Figure 5. TL glow curves of BeO pellets calcinated at 900 °C for different durations.

3.3. OSL Decay Curves

Fig. 6. shows OSL decay curves of 0.5 Gy irradiated BeO pellets which was calcinated at different temperatures of 800, 900, 1000, 1100 and 1200 °C for 4 h. After a preheat treatment of 100 °C for 10s, the OSL decay curves were obtained with blue light stimulations throughout 200 s. As seen from Fig. 6., the maximum OSL signal intensity was obtained from the BeO pellets calcinated at 900 °C as for RL and TL signals. In order to see more clearly the total trapped charge population, inset Fig. 6. provides integrated OSL signals obtained by collecting data from 0 to 200 s against the calcination temperature. As results obtained from the maximum OSL signals, the total charge population gave the maximum value for the sample calcined at 900 °C because the structure of the OSL decay curves did not change. In addition to calcination temperature study, OSL decay curves were obtained from the BeO pellets calcinated at 900 °C for different durations of 2, 4, 6, 8, 10, and 24 h (see Fig. 7). As seen from Fig. 7., the maximum OSL signal intensity was obtained from the BeO pellets calcinated at 1000 °C for 4 h. Considering the total trapped charge population from a different perspective, the integrated OSL signals were presented in inset Fig.7. against the calcination durations. Considering all the OSL decay curves of BeO samples, the OSL signals gave the maximum value for the sample calcined at 900 °C for 4 h because different calcination conditions do not change the structure of OSL traps in BeO.

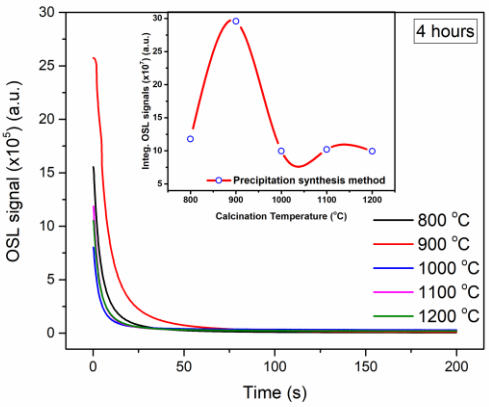

Figure 6. OSL decay curves of BeO pellets calcinated at different temperatures for 4 h. Inset: Integrated OSL signals of BeO pellets calcinated at different temperatures for 4 h.

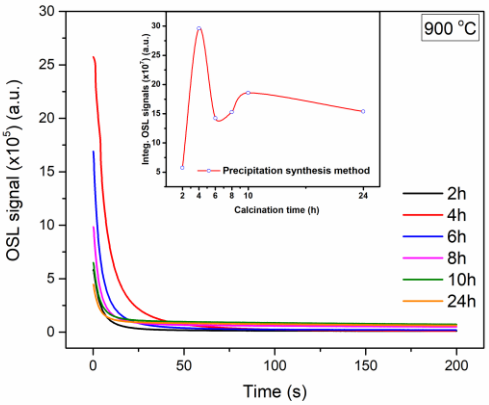

Figure 7. OSL decay curves of BeO pellets calcinated at 900 °C for different durations. Inset: Integrated OSL signals of BeO pellets calcinated at 900 °C for different durations.

4. Conclusions

Undoped BeO powders were synthesized using the precipitation method and prepared as a ceramic pellet. All the RL emissions are in good agreement with previously reported emissions. All the obtained RL emissions show the same broad highly sensitive emission peak located between 200 and 500 nm. Unexpected large emission peaks located between 700 and 800 nm are associated with the oxygen defects in BeO may act as anion defects occurring during synthesis in the structure. According to TL and OSL results, the appropriate calcination temperature and duration were 900 °C, 4h for BeO pellets which were synthesized using precipitation method. It was clearly demonstrated that TL and OSL signals can be used in radiation dosimetry applications. In future studies, more dosimetric properties of the material should be examined using TL and OSL methods for different calcination conditions.

Acknowledgements

This project has been supported by the Çukurova University Rectorate through the project FDK-2018-10190. We are grateful to Çukurova University Rectorate for their supports. We appreciate Prof. Kasım Kurt for RL measurements.

References

[1] Rivera, T. (2011). Synthesis and thermoluminescent characterization of ceramics materials. Advances in ceramics–synthesis and characterization, processing and specific applications. InTech, Rijeka, Croatia, 127-164.
[2] Boch, P., & Niepce, J.-C. (2010). Ceramic Materials: Processes, Properties, and Applications (Vol. 98): John Wiley & Sons.
[3] Carter, C. B., & Norton, M. G. (2007). Ceramic materials: science and engineering (Vol. 716): Springer.
[4] Albrecht, H. O., & Mandeville, C. E. (1956). Storage of Energy in Beryllium Oxide. Physical Review, 101(4), 1250-1252. doi:10.1103/PhysRev.101.1250
[5] Rhyner, C. R., & Miller, W. G. (1970). Radiation dosimetry by optically-stimulated luminescence of BeO. Health Physics, 18, 681-684.
[6] Tochilin, E., Goldstein, N., & Miller, W. (1969). Beryllium oxide as a thermoluminescent dosimeter. Health Physics, 16(1), 1-7.
[7] McKeever, S. W., Moscovitch, M., & Townsend, P. D. (1995). Thermoluminescence dosimetry materials: properties and uses.
[8] Bulur, E., & Goksu, H. Y. (1998). OSL from BEO ceramics: New observations from an old material. Radiation Measurements, 29(6), 639-650. doi:Doi 10.1016/S1350-4487(98)00084-5
[9] Bos, A. J. J. (2001). High sensitivity thermoluminescence dosimetry. Nuclear Instruments & Methods in Physics Research Section B-Beam Interactions with Materials and Atoms, 184(1-2), 3-28. doi:Doi 10.1016/S0168-583x(01)00717-0
[10] Sommer, M., & Henniger, J. (2006). Investigation of a BeO-based optically stimulated luminescence dosemeter. Radiat Prot Dosimetry, 119(1-4), 394-397. doi:10.1093/rpd/nci626
[11] Sommer, M., Jahn, A., & Henniger, J. (2008). Beryllium oxide as optically stimulated luminescence dosimeter. Radiation Measurements, 43(2-6), 353-356. doi:10.1016/j.radmeas.2007.11.018
[12] Jahn, A., Sommer, M., Ullrich, W., Wickert, M., & Henniger, J. (2013). The BeOmax system – Dosimetry using OSL of BeO for several applications. Radiation Measurements, 56, 324-327. doi:10.1016/j.radmeas.2013.01.069

[13] Altunal, V., Guckan, V., Ozdemir, A., Sotelo, A., & Yegingil, Z. (2019). Effect of sintering temperature on dosimetric properties of BeO ceramic pellets synthesized using precipitation method. Nuclear Instruments and Methods in Physics Research Section B: Beam Interactions with Materials and Atoms, 441, 46-55.

[14] Altunal, V., Guckan, V., Ozdemir, A., Can, N., & Yegingil, Z. (2019). Luminescence characteristics of Al-and Ca-doped BeO obtained via a sol-gel method. *Journal of Physics and Chemistry of Solids*.doi: https://doi.org/10.1016/j.jpcs.2019.04.003

Journal of Investigations on Engineering & Technology
Volume 2, Issue 2, 26-12, 2019
ISSN: 2687-3052

Structure characterization and luminescence studies of MgO:Li calcinated at different temperatures via solution combustion and sol-gel methods

Veysi GUCKAN[1*], Volkan ALTUNAL[1], Adnan OZDEMIR[1], Zehra YEĞİNGİL[1]

1Department of Physics, Faculty of Art and Sciences, 01330 Balcali Saricam, Adana, Turkey

(Received: 23.10.2019, Accepted: 25.12.2019, Published Online: 26.12.2019)

Keywords
Thermoluminescence
Photoluminescence
MgO
Calcination

Abstract: In the present study, lithium (Li) doped magnesium oxide (MgO) samples were prepared using Solution Combustion Synthesis (SCS) and Sol-Gel (SG) methods. Their photoluminescence (PL) and thermoluminescence (TL) behaviors were determined after the different calcination temperatures. The aim of this study is to investigate the effect of different calcination temperatures on the PL and TL sensitivities of lithium doped MgO (MgO:Li) samples in pellet and powder forms prepared by SCS and SG methods. The structural characterization analysis of MgO:Li powder and pellets were carried out using X-ray diffraction (XRD) and scanning electron microscope (SEM) methods. The results of these structure analysis showed that MgO:Li samples have different crystal properties when changing calcination temperatures were applied during the preparation of the samples. Luminescence properties of the MgO samples which were synthesized at different calcination temperatures were investigated by the Photoluminescence (PL) and TL techniques. The maximum TL intensity of the samples was obtained at a calcination temperature of 800 and 1000 oC for the SCS and SG methods, respectively. Uncontrolled chromium impurities were observed in MgO samples by using PL measurements. On the PL spectrum, peaks indicating chromium (III) (Cr3+) transmission in the red portion of the spectrum at 672, 698 and 721 nm are clearly evident. We investigated high dose sensitivity in these samples. This study presents optimum calcination temperatures in order to obtain maximum PL and TL sensitivity of MgO sample. It is also clear that it will contribute to the literature that it can be studied as a new dosimetric material.

1. Introduction

Magnesium oxide (MgO) is a wide band-gap (E_g=7.8 eV) insulator under ambient pressure. MgO has high chemical and thermal stability, and high surface reactivity. These properties make it a promising material for application in sensors, catalysis, paints, and additives (Shukla et al., 2004). MgO has a high melting point of about 2800 ^oC. Its density is about 3.58 g/cm^3 and the Mg ions occupy the octahedral sites within the anion close-packed structure (Klein & Hurlbut Jr, 1999).

MgO has long been accepted as a luminescence dosimetry material, mainly for use with the thermoluminescence (TL) technique. In order to increase the number of materials suitable for optically stimulated luminescence (OSL) dosimetry, many researchers have investigated the luminescence characteristics of this material (Bos, Prokić, &

*İlgili yazar: veysiguckan@gmail.com ORCID: 0000-0001-7693-7770

Brouwer, 2006; Oliveira, Doull, & Yukihara, 2013; Oliveira, Milliken, & Yukihara, 2013). There are many reports of MgO doped with lanthanides or transitions metal ions to increase the TL or OSL signals and to improve its dosimetric characteristics (Oliveira, Doull, et al., 2013; Oliveira, Yukihara, & Baffa, 2019; Yukihara et al., 2013).

In this study, the effect of calcination conditions on TL and OSL intensities of MgO phosphors produced by the SCS and SG methods were presented. Li-ion was doped into the MgO phosphors during the synthesis process as dopants and different calcination temperatures and times were performed to obtain high sensitivity MgO luminophors that can be for TL and CW-OSL dosimeters. The structure and morphology of the synthesized materials were checked by XRD and SEM methods. The TL and OSL curves of Li doped MgO phosphors calcinated at different temperatures and times were compared with each other.

2. Materials and methods

Material preparation

This study presents the calcination effect on MgO samples in pellet form prepared by SCS and SG methods. All chemicals were supplied from Sigma Aldrich. Li was used as the dopant with 0.1% mol for both methods. The calcination temperatures and times used in both production methods are 800, 900, 1000, 1100 and 1200 ^{o}C for 2, 4, 6, 8, 10 and 24 hours. After the bulk material was produced, the material was divided into 5 equal parts and then calcined at different temperatures, keeping the time constant for 4 h. In this work, MgO samples were studied in pellet form for having more settled PL and TL signals and for easy handling. MgO pellets were performed as a 6 mm diameter and 0.6 mm thickness as a shape of disk form using 25 milligrams calcinated powders. In all TL measurements, readings were taken after the sintering of all types of pellets at 1600 oC for 4h. The calcination temperature giving the best TL signal was selected and the time experiment was performed (It is not given). The same process was repeated for the time experiment.

Characterization

A few characterization analyses of MgO samples obtained by SCS and SG methods were performed. All of the analysis was performed at the room temperature. The phase evaluation and crystal structure characteristics of pellet-shaped MgO samples were studied by means of the XRD technique. The measurements were performed using XRD PANalytical EMPYREAN branded diffractometer equipped a copper and cobalt X-ray tube, and copper Kα radiation wavelength was 0.1541 nm. Diffraction angles were adjusted from 20° to 90° (scan mode, Δ2θ=0.02°). Qualitative phase analyzes were performed by comparison of the experimental diffraction patterns with the standard ones from the International Centre for Diffraction Data (ICDD). The surface morphology of the samples and microstructures of MgO pellets were examined using a FEI branded Quanta 650 model field-emission SEM with 30–100 kV accelerating voltage and 100nA probe current.

Luminescence measurements

PL measurements were performed using a monochromatized xenon lamp as the excitation source. All PL spectra were obtained at room temperature. The PL and PLE spectra were measured using a Horiba/Jobin-Yvon Fluorolog-3 spectrofluorimeter. It has a continuous xenon lamp (450 W) and a photomultiplier tube (Hamamatsu R928P). The measured PLE spectra were corrected by the xenon lamp emission spectrum.

TL measurements were carried out using a Risø TL/OSL reader model DA-20 (Risø National Laboratory, Denmark). Luminescence emission were measured in the VIS region using a Schott BG-39 filter (300–700 nm) and UV region using a bandpass filter (Hoya, U-340, transmittance range from 250 to 390 nm, max 340 nm) in front of the PM tube. In order to the detection of light, a bialkali photomultiplier tube (PMT) was used (model 9235QB, Electron Tubes Ltd., Uxbridge, UK). Samples were irradiated at room temperature using an in situ 90Sr/90Y beta source. This ionizing irradiation source emits beta particles with a maximum energy of 2.27 MeV. All TL measurements were performed at a heating rate of 5 ^{o}C/s.

3. Results

Crystallographic characterization and morphology of the samples were studied by XRD and SEM. The XRD pattern of Li doped MgO pellets are given in Fig. 1. Fig. 1 shows that the pattern matched well with ICDD 98-064-2714 in terms of peak positions indicating the formation of single phase. It has cubic structure with lattice parameters of a =b=c=4.2080 Â. XRD spectra of all MgO:Li pellets having the diffraction peaks (111), (200), (220), (311) and (222) located at 2theta = 36.9°, 42.9°, 62.3°, 74.7°and 78.7°, respectively. It was observed that the different calcination temperatures applied did not cause any difference in the phase in the crystallographic structure.

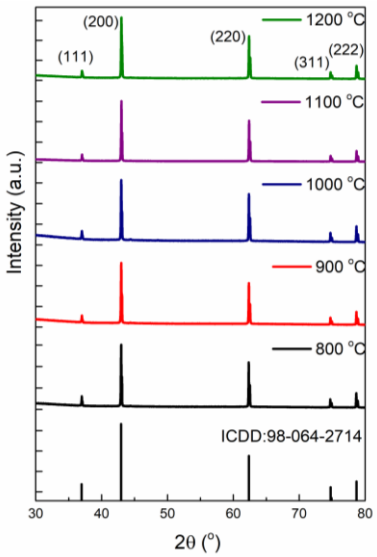

Figure 1. XRD analysis of MgO:Li pellets calcinated at different temperatures.

The SEM images revealed the morphological characteristics of Li doped MgO pellets produced by sol-gel methods. The SEM images of produced samples are shown in Fig. 2. There is homogeneous distribution among particles for all the MgO:Li pellets. These images do not clearly show us how the calcination temperature creates differences in the morphology of the MgO pellets. It needs further studies.

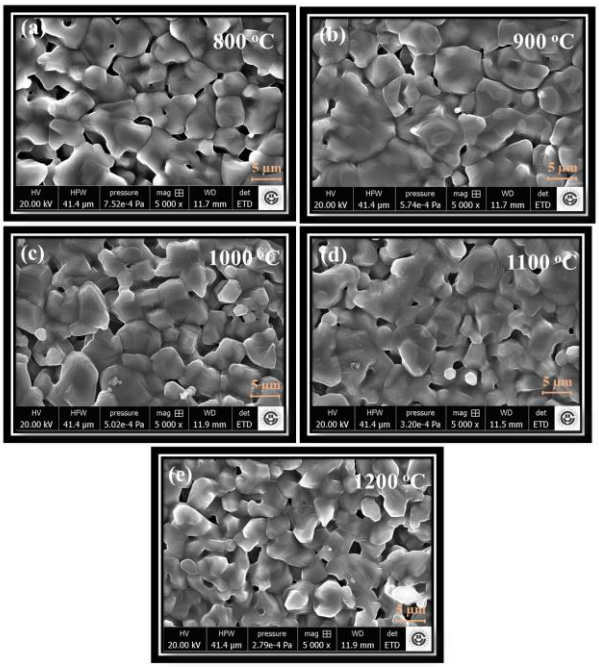

Figure 2. The typical SEM images of MgO:Li pellets calcinated at; (a) 800 °C, (b) 900 °C, (c) 1000 °C, (d)1100 °C and (e) 1200 °C for 4 h

The room temperature photoluminescence emission spectrum of MgO:Li pellets prepared by combustion and sol-gel methods excited with a wavelength of 330 nm were shown in Fig. 3. MgO:Li pellets prepared using the SCS method have a broad emission peak centered at ~660 nm (1.88 eV, orange region). The pellets produced using the sol-gel method have both a relatively narrow peak at 660 nm and a peak at 720 nm in some of the samples. Interestingly, uncontrolled chromium impurities were observed in MgO samples. When the samples excited with 440 nm, peaks indicating chromium (III) (Cr^{3+}) transmission in the red portion of the spectrum at 672, 698 and 721 nm are clearly evident (see Fig. 4) [1, 2].

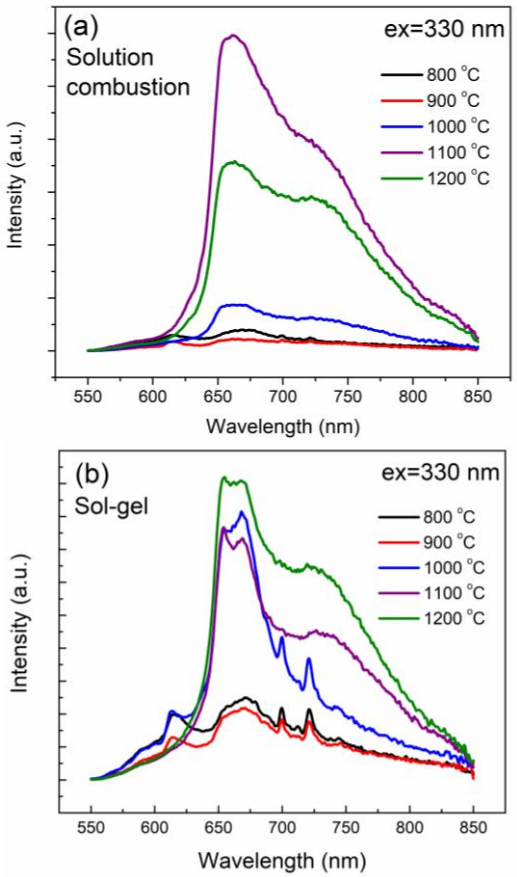

Figure 3. The PL spectra of the MgO:Li pellets

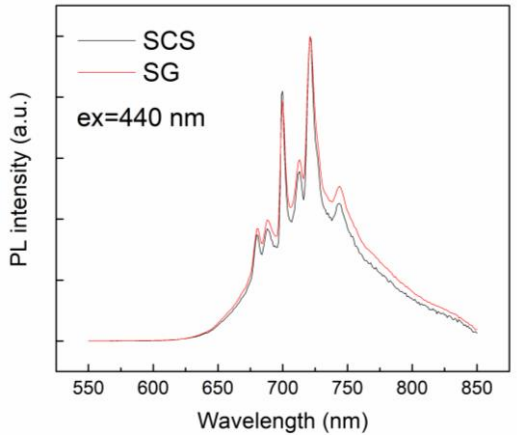

Figure 4. The PL spectra of the MgO:Li pellets under 440 nm excitation.

Fig. 5 shows the TL glow curves from MgO:Li pellets after 2 Gy beta irradiation in comparison with

calcinated samples at different temperatures. TL readouts were performed by heating each sample from room temperature up to 450 °C with a heating rate of 5 °C/s. As is seen in Fig. 4a, maximum trapped charge populations were obtained from MgO:Li pellets prepared using SCS method with calcination temperature at 800 °C for 4 h. Fig. 4b shows that the maximum intensities of MgO:Li pellets were recorded from samples calcinated at 1000 °C for 4 h.

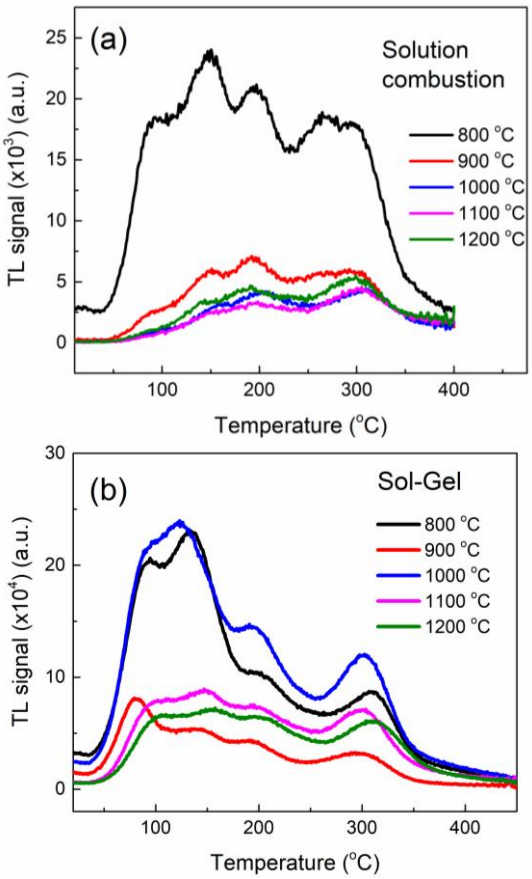

Figure 5. The TL glow curves from MgO:Li pellets prepared using (a) solution combustion method and (b) sol-gel method calcinated at 800 °C, 900 °C, 1000 °C, 1100 °C and 1200 °C for 4 h.

4. Conclusion

Li doped MgO pellets produced using solution combustion synthesis and sol-gel methods were verified by XRD measurements. MgO samples did not contain different phases were highly compatible with the reference number ICDD 98-064-2714 in terms of peak positions. SEM images showed that all samples were homogeneous with no hollow structure between the grains. According to TL measurements, for the Li doped MgO samples prepared using SCS and SG methods, the maximum trapped charge populations were obtained from MgO:Li pellets with calcination conditions of 800 °C. and the maximum intensities of MgO:Li pellets were recorded from samples calcinated at 1000 °C, respectively. However, it is evident that the trap structures formed in the material could not be formed at high energy levels by the dopants. Therefore, TL peaks were obtained at temperatures lower than desired. It was observed that the change in calcination temperature did not affect the TL glow curve. It is clear that the effect of calcination temperature on TL signals needs further study.

Acknowledgements

This research was partly funded by the Cukurova University Research Projects Development and Coordination Unit under the project numbers FDK-2018-10599. We thank Cukurova University for supporting the project.

References

[1] Bos, A., Prokić, M., & Brouwer, J. (2006). Optically and thermally stimulated luminescence characteristics of MgO: Tb3+. *Radiation Protection Dosimetry, 119*(1-4), 130-133.

[2] Klein, C., & Hurlbut Jr, C. (1999). Manual of Mineralogy. John Wiley & Sons. *Inc., New York*.

[3] Oliveira, L., Doull, B., & Yukihara, E. (2013). Investigations of MgO: Li, Gd thermally and optically stimulated luminescence. *Journal of Luminescence, 137*, 282-289.

[4] Oliveira, L., Milliken, E., & Yukihara, E. (2013). Development and characterization of MgO: Nd, Li synthesized by solution combustion synthesis for 2D optically stimulated luminescence dosimetry. *Journal of Luminescence, 133*, 211-216.

[5] Oliveira, L., Yukihara, E., & Baffa, O. (2019). Lanthanide-doped MgO: A case study on how to design new phosphors for dosimetry with tailored luminescent properties. *Journal of Luminescence*.

[6] Shukla, S., Parashar, G., Mishra, A., Misra, P., Yadav, B., Shukla, R., . . . Dubey, G. (2004). Nano-like magnesium oxide films and its significance in optical fiber humidity sensor. *Sensors and Actuators B: Chemical, 98*(1), 5-11.

[7] Yukihara, E., Milliken, E., Oliveira, L., Orante-Barrón, V., Jacobsohn, L. G., & Blair, M. (2013). Systematic development of new thermoluminescence and optically stimulated luminescence materials. *Journal of Luminescence, 133*, 203-210.

Journal of Investigations on Engineering & Technology
Volume 2, Issue 2, 26.12, 2019
ISSN: 2687-3052

Effect of Rb Substitution on the Structural, Physical and Superconducting Properties of Bi-2212 Superconductor

İbrahim ERGİN*[1], Bekir ÖZÇELİK[1], Andres SOTELO[2], M.A. MADRE[2]

[1]Çukurova Üniversitesi, Fen-Edebiyat Fakültesi, Fizik Bölümü, 01330, Adana, Türkiye
[2] *ICMA (CSIC-Universidad de Zaragoza). María de Luna*, 50018, Zaragoza, İspanya

(Received: 24.10.2019, Accepted: 25.12.2019, Published Online: 26.12.2019)

Keywords
Bi-2212
Rubidium substitution
Magnetic Properties

Abstract: In this research, the effects of Rubidium (Rb) inclusion on the microstructural, physical and superconducting properties of $Bi_2Sr_2Ca_{1-x}Rb_xCu_2O_{8+y}$ with x=0.0, 0.025, 0.05, 0.075, 0.10, and 0.125, superconductor have, in detail, been studied. For this purpose, the samples were prepared through the classical solid state reaction route. From the XRD patterns, the crystal symmetries of samples were determined as pseudo tetragonal and consist of dominant Bi-2212 phase together with small amount of secondary phases. SEM-EDX results have confirmed that the major phase is related to Bi-2212, with minor amounts of secondary phases. In magnetization versus temperature measurements, very sharp diamagnetic transition is observed. The superconducting critical temperatures, T_C, for all samples are obtained around 80 K. From *M-H* measurement, it has been found that all samples have very narrow loop areas. By using the data from *M-H* measurements in the Bean model, the intragranular critical field, J_C, has been determined. It has been found that the pure Bi-2212 (x=0.0) sample shows the highest superconducting properties and the largest J_C values (2,2x10^4 A/cm^2 at 10 K).

1. Introduction

Bi-based superconductors with Bi-Sr-Ca-Cu-O (BSCCO) content and stoichiometric 2-2-1-2 respectively are called Bi-2212, which are into the high-temperature superconductor structure. It is too easy to produce in terms of their oxidized structure and contain no rare earth elements and is not easily affected by oxygenated environments. Moreover, it has high current carrying capacity, high magnetic field carrying capacity and the high transition temperature to superconductivity makes this type of superconductor more attractive in industry. However, mechanical properties such as weak bonds, brittleness and weak elasticity in the structure of this superconductor family restrict their application. The BSCCO superconductor family with a chemical structure has n = 1, 2 and 3 phase structures (Bi-2201, Bi-2212 and Bi-2223 respectively) depending on CuO_2 content [1-3].

It has been stated the superconducting properties of the BSCCO system can be improved by alkaline metals substitutions, since their +1 valence state generates a variation in the charge carrier concentration. In addition, their ionic radii, ranging in between 73–181 pm, superpose with the Bi, Sr, Ca, and Cu ones [4-6]. In this work, the optimum amount of Rb substitution into BSCCO system by replacing Ca will be determined through the variation of structural, physical and magnetic properties of the doped systems as a function of Rb-concentration.

2. Experimental Details

$Bi_2Sr_2Ca_{1-x}Rb_xCu_2O_y$ samples were produced by solid state method at x = 0.0, 0.025, 0.05, 0.075, 0.1, and 0.125 combinations. Oxidized and carbonate powders used are Bi_2O_3, $SrCO_3$, $CaCO_3$, Rb_2O and CuO. Oxidized and carbonate powders were mixed separately for each sample. The mixtures were well mixed by milling in an agate mortar and calcined twice at 750 and 800°C for 12 h in order to decompose the alkaline-earth carbonates. The purpose of the calcination course is to ensure the decomposition of carbonated structures. The carbonated structures are

*İlgili yazar: erginibrahim2@gmail.com ORCID: 0000-0002-6778-5442

separated during the sintering process after calcination and can form bubble structures. In this case it may have a slowing or stopping effect on the formation of the desired crystal structure. Rigaku Minifilex, XRD device, which emits CuKa radiation at a certain ratio of 10 to 70 degrees (2θ) at room temperature as powder, was used to determine the phases in the heat treated material. From these phases, crystal lattice parameters were calculated with an uncertainty of ± 0.001. For surface morphology and elemental analysis, LEO Evo-40 VPX scanning electron microscopy (SEM) and energy dispersive spectroscopy (EDS) were used. For magnetic measurements, the 7304 model Vibrating Sample Magnetometer of Lake Shore was used to determine the transition temperature to superconductivity and to observe the magnetization change in the ±1 Tesla magnetic field.

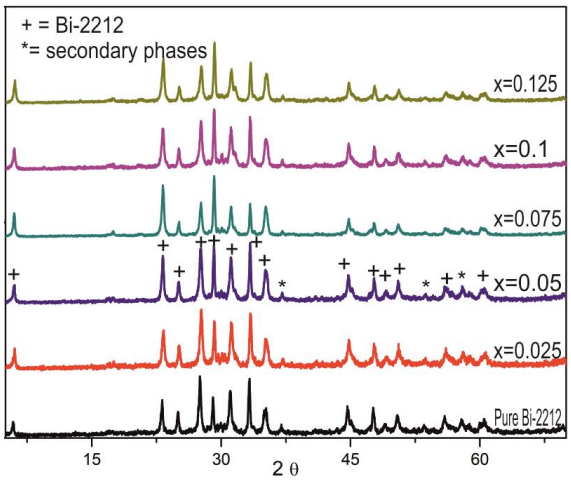

Fig. 1. XRD patterns for all samples with increasing Rb concentration from bottom to top

3. Result and Discussion

As can be observed from XRD patterns given in Fig.1, the main phase labeled as (+) is Bi-2212 one together with minor phases (*), for all different Rb-substitution. As can be seen from the XRD results, Rb entered Bi-2212 phase due to none existence of Rb content peaks. The crystal symmetry is found as pseudo tetragonal with the lattice parameters, calculated by using the least squares method, are a=b=5.398 Å and c=30.685 Å, in all cases.

Fig. 2 shows the phases according to the specific contrast setting on the material surface. The identities of the phases are determined according to the elemental analysis (EDX) at the places marked with 1, 2 and 3. EDS analysis of these contrasts has allowed to associate each of them to different phases: major gray contrast (indicated by #1) in all micrographs corresponds to the Bi-2212 superconducting phase, while white (#2) and dark gray (#3) have been associated to $Bi_{2+x}(Sr,Ca)_2O_{6+d}$ (without Cu phase), and $(Sr,Ca)CuO_2$ (without Bi phase) secondary phases, respectively.

Magnetization, M, versus temperature is exhibited in Fig. 3, for all samples. All data were generated in a cooled mode under magnetic field from 20 K to 100 K under 100 Oe magnetic field. By increasing the sensitivity in a temperature range close to the transition temperature, T_C, it is provided to determine the transition temperatures to an exact value. From the M-T graph, the critical transition temperatures for all samples were deduced in a very similar way. It can be seen from Table 1 that all samples, regardless of the concentration of the Rb additive, have a critical transition temperature of around 80 K.

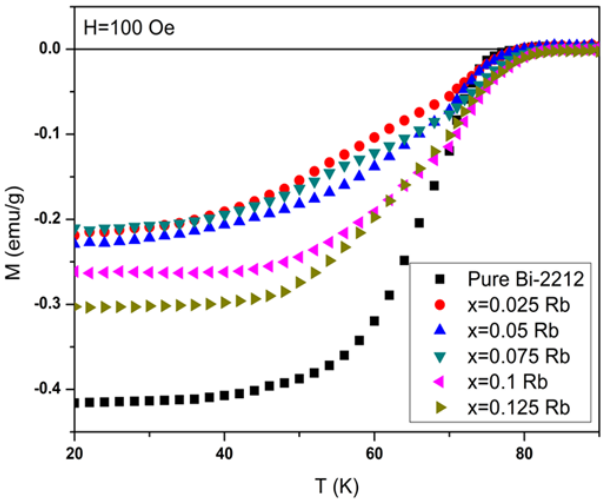

Fig. 3. Magnetization (M) versus temperature (T), for all samples.

It is likely that diamagnetic behavior makes it difficult to infiltrate the magnetic field between these grain boundaries due to the strong connection between the grain boundaries.

The M–H loops measured at 10 K, between ±1 Tesla applied external fields, and determined under ZFC mode, are presented in Fig. 4. All samples exhibit very narrow hysteresis and the area of these hysteresis loops decrease depending on concentration. M-H data were used in Eq. 1, proposed for quadrangular samples, in the well-known critical Bean model [7]

$$J_C = 20\frac{\Delta M}{a(1-\frac{a}{3b})} \qquad (1)$$

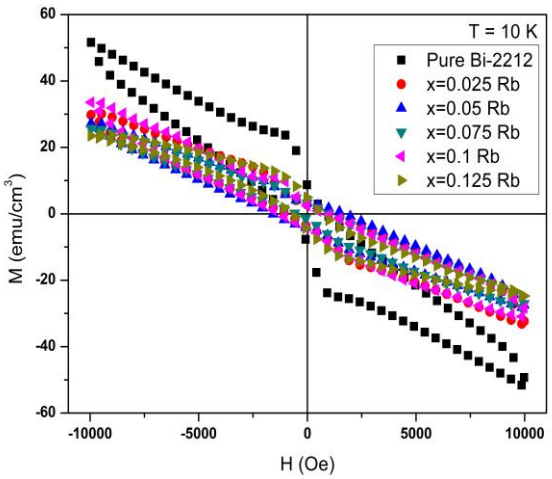

Fig. 4. Magnetization, *M*, versus magnetic field, *H*, for all samples

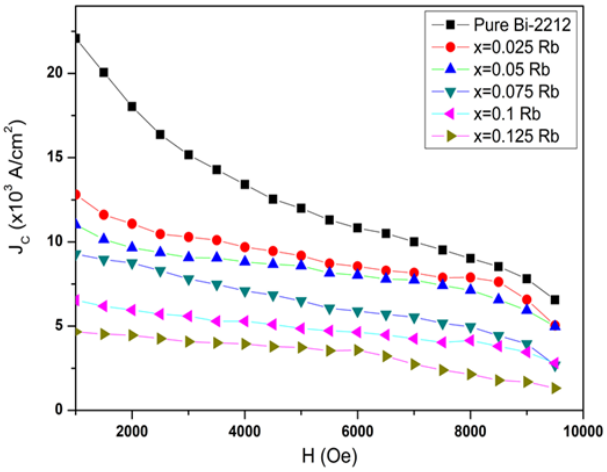

Fig.5. Critical current density, J_C, versus magnetic field, *H*, for all samples.

Table 1. Critical transition temperature, T_C, for all samples

Samples	T_C (K)
x=0	80
x=0.025	78.6
x=0.05	80.3
x=0.075	79.5
x=0.1	79
x=0.125	82

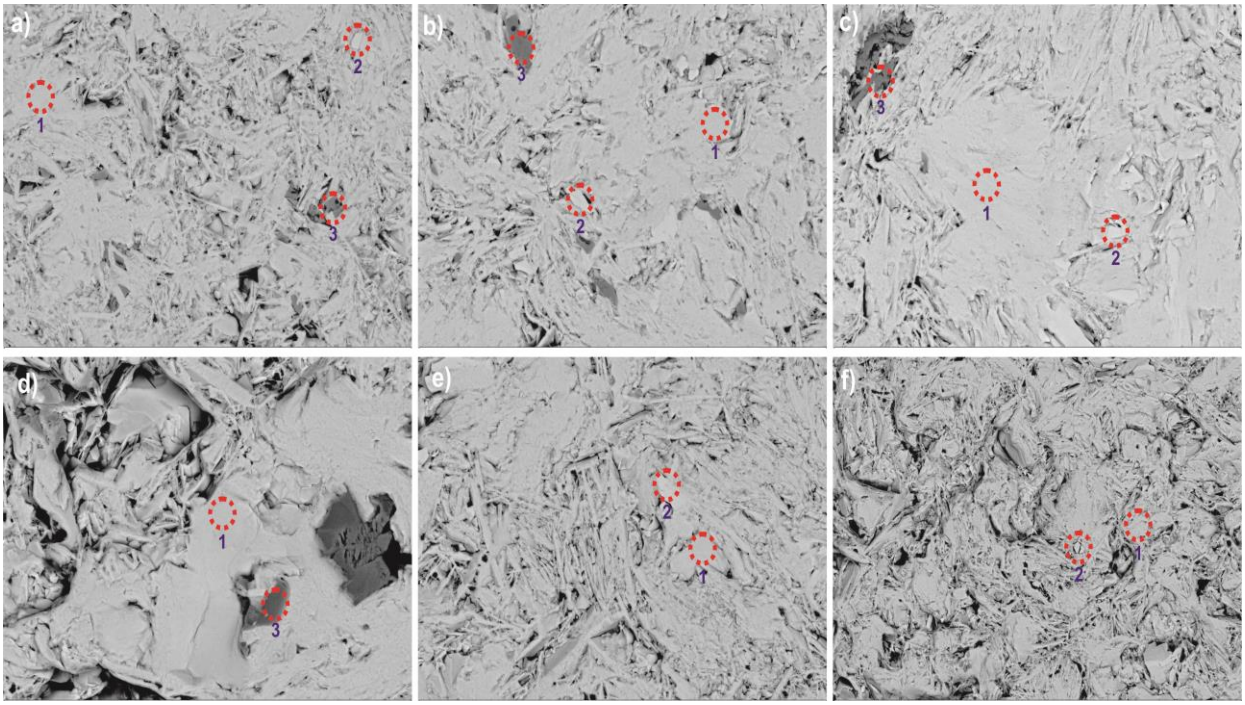

Fig. 2. SEM micrographs for all samples. (a) x=0.0, (b) x=0.025, (c) x=0.05, (d) x=0.075, (e) x=0.1, (f) x=0.125

where $\Delta M = M_+ - M_-$ is measured in electromagnetic units per 200 Oe, *a* and *b* are the length of the sample plane perpendicular to the applied magnetic field. Using the Eq.1, the intragranular critical current density values, *Jc*, in ampéres per square centimeter are calculated for all samples, and the results obtained at 10 K are presented in Fig. 5. These data clearly show that the pure sample (x=0.0) possesses higher superconducting properties and has the largest J_C values ($2{,}2 \times 10^4$ A/cm^2 at 1000 Oe fields), which explicitly reduce when the magnetic field and the amount of Rb are raised. In this stage, it is possible to argue that the different type of secondary phases embedded in the crystal structure can reveal such a kind of results. According to the flux-pinning mechanism, those non-superconducting phases.

4. Conclusions

In summary, the structural, physical and magnetic properties of $Bi_2Sr_2Ca_{1-x}Rb_xCu_2O_{8+y}$ superconducting material with x=0.0, 0.025, 0.05, 0.075, 0.10, and 0.125 has been intensively studied. X-ray diffraction patterns indicate that all samples have main Bi-2212 phase. SEM micrographs and EDX results have shown that Bi-2212 was major phase with minor amounts of secondary phases. Diamagnetic transitions typical for granular materials were observed, when measuring magnetization versus temperature. The critical onset temperatures were around 80 K, independently of Rb content. *M-H* measurements have shown that the hysteresis loops are very narrow. The critical current field, J_C, of pure sample was found the highest value as $2{,}2 \times 10^4$ A/cm^2.

Acknowledgements

M. A. Madre, and A. Sotelo acknowledge the MINECO-FEDER (MAT2017-82183-C3-1-R), and Gobierno de Aragon-FEDER (Research Group T 54-17 R) for funding. The authors wish to acknowledge the use of Servicio General de Apoyo a la Investigación-SAI, Universidad de Zaragoza.

behave like very effective flux-pinning centers. Depending on the sizes of those secondary phases, the applied fields may diffuse into the sample, causing a decline in the critical current, *Jc*, values. The maximum *Jc* value obtained for the x=0.05 sample is almost near with the given in literature for Vanadium (2.53×10^5 A/cm^2) [8], and very similar to the obtained in Cs-substituted materials ($2{,}3 \times 10^4$ A/cm^2) [9]. This effect may be associated to the different cation sizes affecting the oxygen quantity and the number of charge carrier. In addition, comparison to Na-doped materials, a possible slight charge carrier concentration enhancement can be arisen by the lower effective attraction of the external electrons in the Rb^+ cations [10].

References

[1] H. Maeda, Y. Tanaka, M. Fukutumi, T. Asano, Jpn. J. Appl. Phys. 27, 209 (1988)

[2] C. Michel, M. Herviev, M.M. Borel, A. Grandin, F. Deslands, J. Provost, B. Raveav, Z. Phys. B 86, 421 (1987)

[3] J.M. Tarascon, W.R. McKinnon, P. Barboux, D.M. Hwang, B.G. Bagley, L.H. Greene, G.W. Hull, Y. LePage, N. Stoffel, and M. Giroud, Phys. Rev. B, 1988. 38(13): 8885-8892.

[4] B. Ozcelik, M. Gursul, A. Sotelo, M. A. Madre, J. Mater. Sci. Mater. Electron. 26, 441 (2015)

[5] B. Ozcelik, M. Gursul, A. Sotelo, M. A. Madre, J. Mater. Sci. Mater. Electron. **25**, 4476 (2014)

[6] L.D. Sykorova, O. Smrckova, V. Jakes, Phys. Stat. Sol. (C) **1**(7), 1952 (2004)

[7] C. P. Bean, Phys. Rev. Lett., 8, 250 (1962)

[8] Nane, O. & Özçelik, B. J Mater Sci: Mater Electron (2016)27:7633. https://doi.org/10.1007/s10854-016-4747-3

[9] I. Ergin, B. Özçelik, M.A. Madre, A.Sotelo, J Supercond.Nov.Magn. https://doi.org/10.1007/s10948-019-05150-4

[10] Özçelik, B., Gürsul, M., Sotelo, A. et al. J Mater Sci: Mater Electron (2015) 26: 441. https://doi.org/10.1007/s10854-014-2419-8

Journal of Investigations on Engineering & Technology
Volume 2, Issue 2, 26.12. 2019
ISSN: 2687-3052

Historical Stone Arch Bridges' Damage Causes and Repair Techniques

Yusuf YANIK*[1], Temel TÜRKER[2b], Berna ÇORUHLU[2c], Gonca Kamber YILMAZ [1a]

[1]Karadeniz Technical University, Of Technology Faculty, Civil Engineering Department, 61830, Trabzon
[2]Karadeniz Technical University, Faculty of Engineering, Civil Engineering Department, 61080, Trabzon

(Received:29.08.2019, Accepted:25.12.2019, PublishedOnline:26.12.2019)

Keywords
Arch bridges
Damage causes
Repair methods

Abstract: Many historical stone arch bridges have been exposed to the different environmental effects, which could cause structural damage, at different times. Under these natural or human-induced effects such as floods, earthquakes, the bridges were partially or completely damaged. The repair of the historical arch bridges has been repaired against to these damages. The success of the repair work depends on both a detailed archaeological-historical survey and a detailed structural evaluation process carried out together. It is very important to determine the answers to questions such as date and time of construction of the structure, whether there was any interruption in the construction process, the scheme and the order of the damages of the structure, what were the repairs and strengthening done in the structure and whether there was any change in the use of the environment. After these process, the repair method is determined considering many alternatives such as partial or complete disassembly for remodeling of the bridge, regional repair or regional strengthening, full strengthening of the upper structure, removal of excess weight over the bridge, balancing of mass and stiffness distribution, improvement of structural interaction between arches and feet, strengthening of foundation system of the bridge. In this study, the repair methods against the damages occurred on the historical masonry arch bridges exposed to different damages have been tried to be evaluated.

1. Introduction

Historical stone arch bridges are structures that play an important role in connecting the past and the future. These historical bridges constitute our cultural heritage. Therefore, historical bridges need to be transferred to future generations safely and in a healthy way. Historical stone arch bridges suffered many damages due to the external effects and misuse caused by them, and the damages resulting from these damages need to be repaired correctly. But while repairing these damages, the main purpose of the historical bridge should be to restore the old strength without disturbing the historical texture.

Erdal carried out his work on the control and maintenance management of bridges. This study examined the types of deterioration in stone bridges [1]. Yucel and Namli, investigated the effect of water and other factors on the distortion around the bridge legs. They determined that the deterioration around the bridge legs was closely related to the river regime, bed material and foot type, and it was necessary to investigate the rivers where the bridges would be built and that the most suitable bridge foot type could be determined under the light of these data. In this study, the measures to be taken against the distortions occurring around the bridge pillar, the changes in the speed and pressure area were examined [2]. Bayraktar et al., examined the effect of finite element model improvement on earthquake behavior of historical bridges. They selected the Sinik bridge in Trabzon for this study. They then compared the experimental and theoretically obtained dynamic characteristics of the bridge. Under the light of these data, they updated the finite element model of the bridge and formed the most realistic model [3]. Ural et al., gave general and statical information about historical arch bridges. They presented structural damage occurring at arch bridges in the Karadeniz region and presented repair-strengthening procedures. They gave repair-strengthening techniques applied on stone arch bridges [4]. Alaboz, carried out studies on the current status of the Architect Sinan bridges in the Marmara region, determining what caused the damage and developing appropriate repair recommendations [5]. Korkmaz et al., conducted a dynamic analysis of the historical stone arched Timisvat Bridge in Rize. They compared the displacement and stress values obtained as a

*Responsible author: yusufyanik@ktu.edu.tr ORCID: 0000-0002-5487-5254
[b] ORCID:0000-0001-5632-693X
[a] ORCID:0000-0002-6894-6076
[c] ORCID:0000-0001-6655-4055

result of the analyzes made in the time domain [6]. Firat and Eren, investigated their effect experimentally by applying different FRP reinforcements on the damaged belts. The reinforcement technique was numerically modeled on the applied belts by means of the structural analysis program. They compared experimental and numerical results [7]. Alpaslan et al., investigated the effect of local stiffness increase on building behavior due to local reinforcement in historical buildings. In their study, they examined the results of dynamic analysis in case of strengthening by applying more rigid material to undamaged, damaged and damaged areas of a historical masonry bridge. In dynamic analysis, they showed that the deteriorated elements in the historical structure affect the structure behavior negatively due to load transfer [8]. Koc, the effects of different FRP reinforcement techniques which can be used in damaged stone arch systems on belt behavior were investigated. The reference belt sample was loaded until failure. Six belt samples other than the reference sample were first damaged by applying 75% of the reference sample collapse load [9]. Ilerisoy and Sagir,. the impacts of bridges that have witnessed history, deterioration and destruction caused were discussed. Studied the factors discussed above in Erzincan Tercan Kotur Bridge [10]. Eren, made experimental investigation of various repairing techniques applied to damaged masonry arches [11].

In this study, natural and overloading of historical stone bridges such as earthquakes, floods, ground damages and over time damages caused by alteration of river bed, damages caused by alteration of bridge slope, wars, faulty repairs were evaluated and repair methods investigated.

2. Damages and Causes of Historical Stone Arch Bridges

Many stone arch bridges that survived to the present day were influenced by structural damage in the process. Bridges were damaged under these natural or man-made effects such as floods and earthquakes. Analysis of design differences and damage-causing mechanisms that cause structures to react differently under the same influences was a priority in the protection and repair of structures. Damages in stone arch bridges were mostly caused by floods, earthquakes and human-caused damages.

2.1. Flood Damage

Our country has located in temperate climate zone. However, rivers with irregular regimes could produce floods that cause significant structural damage to river bed during rainy seasons. The bridges on this route were the most damaged structures from floods [5]. In addition to the water force, the tree trunks that the stream incorporates during the floods also damaged the bridges. Although most of the historical bridges had flood cutters, many arch bridges were damaged due to floods. As a result of the flood of the Ilıcak Bridge in Bitlis, the tempan wall and deck were largely destroyed. The bridge, which was restored in 2005, was completed by KGM in 2006 (Figure 1). The Akcaabat Osmanbaba Bridge was completely destroyed as a result of excessive rain water carving the bridge's feet [12].

Historical Ilicak Bridge

Osmanbaba Bridge

Figure 1. Examples of bridges damaged and destroyed by floods

2.2. Earthquake Damage

Due to the presence of many active faults in our country, it could be affected by destructive earthquakes. The bridges were constructed of stone material with high resistance to pressure stresses. Therefore, it could withstand high stresses under vertical loads. However, they were vulnerable to damage under horizontal forces caused by earthquakes (Figure 2). In order to compensate for these horizontal forces, metal elements could be used which could meet the tensile forces such as tension, clamp and tenon.

Figure 2. Bridges damaged by the 2001 Bhurj earthquake and the Koyna earthquake in India

After the Umbria Marche earthquake in 1997, a major collapse occurred in the central opening was shown in Figure 3.

Figure 3. Injured bridge [13]

2.3. Human damage

Human damage; design errors, wars, changes made for functional purposes, misapplications brought about by information and technical deficiencies [5].

2.4. Damage caused by river bed replacement

Changes in the river bed caused the amount of water to pass through a narrower section to increase the flow rate. This effect would increase to higher levels in flood situations. Since the sand quarries established on the sides of the rivers also had a direct effect on the rivers regime, the amount of granular material carried in the rivers varies and could cause carving on the bridge legs.

2.5. Overload

The stone material and the arch form were very important considering that the compressive force carrying capacity of the bridge arches continued to function smoothly. However, the increase in loads on the fill could cause swelling and collapse of the façade walls, and as a result of overloading, the horizontal forces created by the belt stones could not be compensated and separations could occur in the arch vaults and disintegration of the keystones (Figure 4) [5].

Figure 4. Damage to the historical Dortgoz Bridge on the road route

2.6. Changing the bridge slope

Changing the inclination of the bridge could cause distortion on the structure as it would generate new fill loads to the arches. In addition, the dynamic effects of the vehicle traffic that would pass through it caused damage to the belts and feet.

2.7. Wars

The wars that have been going on for centuries have targeted the works of a culture or civilization and posed a threat to the bridges. Mostar Bridge, dated 1566, was demolished in an attack in 1993 and was rebuilt in 2004.

2.8. Inproper Repairs

Failure to use sufficient knowledge and technical knowledge during repairs or interventions performed without detailed analysis of the structure could cause damage after application [5].

2.8.1. Inappropriate material use

Failure to use appropriate materials in building materials and binder mortars was among the most common repair mistakes. When choosing a building material, the appropriate stone should be selected by taking into consideration the physical characteristics of the original material, the strength and core weight of the material, the void ratio, the capillary water absorption value and the chemical content, the environmental conditions and the relationship with other building materials. Due to the difference in strength, imbalance in the stiffness distribution would result and regional damage would result.

The chemical composition of the building material must have been such that it does not interact with the binder and air it was in contact with. For example, as a result of the use of cement with lime-based stones, moisture in the air could cause new salt compounds in the stone material. The salt compounds formed in the stone cavities could disintegrate the stones due to the increased in volume (Figure 5).

Figure 5. Damage caused by salting and freezing-thawing of stones

2.8.2. Wrong detail application

As with many conventional structures, the failure to apply the details used in the connection of structural elements in bridges could lead to various damages. In bridges, the use of metal elements in the vertical and horizontal directions to connect the stones to each other was common. Stones were made with each other by clamping lead obtained from iron with low carbon content and this process generated ease of application since the lead was placed in liquid state (Figure 6).

During the construction of the arches and walls, care must be taken to ensure that the dimensions of the stones and their interlocking distance, in particular the integrity of the surrounding stones with the arch vaults, were achieved.

Figure 6. Stones and lead castings connected with sutures, Saraçhane Bridge repair

2.8.3. Changing belt form

During some repairs, the arch form were changed consciously or unconsciously. Some faulty repaired not only disrupt the architectural authenticity of the structure, but also changed the static balance of the bridge. Changing the belt shape made the push line more unfavorable than the ideal belt curve (Figure 7).

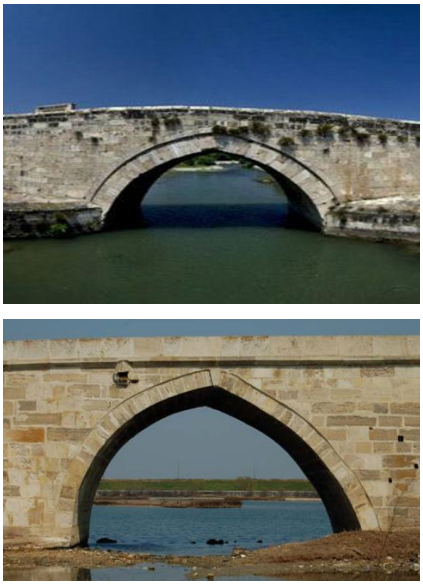

Figure 7. Deformed arch after repair, Buyukcekmece Bridge

2.9. Damages caused by plants

Our country was rich in vegetation because of its abundant rainy. Under the effect of elongation of the roots, plants caused cracking and disintegration of large rock fragments [4]. Weaknesses in the bridge pavement and drainage system also formed the basis for the formation of vegetation (Figure 8). Apart from the plants that damage the structure with their roots, various types of fungi were also fed with minerals such as calcium, aluminum, iron and potassium within the building blocks of the bridge. As a result, acids released the binders on the structure.

Figure 8. Giresun, Dereli road Yavsan Bridge and Savsat Bridge in district of Artvin

2.10. Ground Damage

As a result of the change of direction of the river bed, the carving of the foundations of the bridges occurred. As a result of these engravings, some settlements occurred on the bridges. These settlements could cause cracks and fractures (Figure 9) [4].

Figure 9. Trabzon, Macka road Mataraci Bridge

2.11. Damage depend on time

Among the most important reasons for the damage of arch bridges was temperature differences between day and night and the recurrence of natural phenomena such as wind and rain over time (Figure 10) [4].

Figure 10. Kinali bridge and Ozbek bridge

2.12. Damages due to coating material and drainage problems

Poor coating and drainage system caused surface water to leak into the filling area of the bridge. As a result of this, the filling material was crushed and thrown away from the structure and gaps occurred in the filling (Figure 11). In addition, water leaking into the filler could cause expansion in temperature changes.

Figure 11. Historical Hersan and Ilicak bridges in Bitlis

3. Repair and Strengthening Techniques of Damages at Historical Stone Arch Bridges

Historical stone arch bridges should be constructed in such a way that they did not affect the visuality of the bridge while remaining faithful to its original condition and did not disturb its structural spirit. It was very important to make modeling by making visual and experimental studies before the restoration and reinforcement of historical buildings. The following steps could be followed for these operations.

- Determination of the current situation
- Conducting experimental studies
- Modeling
- Calibrate the initial model to reflect the actual situation

Measures should be taken against damages in historical stone arch bridges. Continuous maintenance of historical bridges could prevent many damages. If necessary, repair and reinforcement was mandatory. The method chosen for repair and reinforcement should be safe, economical, fast and continuous. Considerations in practice:

- If the damage was local, a local repair should be performed.
- If local damage was excessive, a general repair was required.
- If the repair disrupted the aesthetics of the structure, it was more appropriate to perform a hidden repair.
- As repairs and reinforcements changed the rigidity of the system, it would be more accurate to arrange the calculations accordingly.
- Once you decided to repair or strengthen, the project must be designed in accordance with the regulations currently in effect.
- It was important that the contractor undertaking the repair was experienced in this field.
- Repair or reinforcement should be checked under the supervision of technical personnel.

3.1. Injection filling of cracks

Historical stone arch bridges were built under pressure. Bridges which were subjected to strong dynamic effects were weak against tensile stresses and thus cracks occurred in the vertical direction due to tensile stresses. The direction and shape of these cracks were very useful in determining the causes of damage.

Cracks in stone arch bridges should be filled by injection. Before the injection, the crack must be revealed by removing the previously made plaster. Afterwards, hoses should be placed at certain intervals (approximately 50-100cm) on the cracks based on the crack width and covered with hydraulic lime material that would not leak over the crack. After a minimum of 24 hours, the appropriate material must be injected into the crack using the injection pump to remove the damage. Injection material should be applied at the lowest point and should not be stopped until it reaches the upper point (Figure 12).

Figure 12. Injection application

3.2. Making anchors with steel bars

In case of disintegration between the stones, it was ensured that the stones were interlocked together by the method applied with steel bushes or anchors (Figure 13).

Figure 13. Use of steel tenon

Horizontal anchorage could prevent the progression of cracks. This process opened the cylindrical slots along the full width of the bridge to the belt side faces respectively. Sheath pipes and stainless steel bars with permeable grout mortar were placed in the opened slots. The low pressure graut mortar was pumped into the sheath pipe. The tension force was applied to the stainless steel bars with a torque wrench. The hole heads were closed (Figure 14) [14].

Figure 14. Horizontal anchorage application [15]

3.3. Partial completion of demolished sections

Reconstruction was a special case. In order to rebuild the damaged area, documents such as technical data, survey, photo of the department to be built were needed. In the light of these data, point intervention method could be applied in the collapsed parts of the bridge. The high water permeability and flowering resistance of the mortars to restore the destroyed parts was important for the future (Figure 15).

Figure 15. Reconstruction of the demolished part with mortar

One of the types of damage often seen in historical arch bridges was the large destruction of side railings. One of the weakest parts of the bridges was the railing stones, which were built in one row. In addition, due to pedestrian and vehicle traffic, some cracks, abrasions and abrasions occurred in the superstructure of the bridge. Guardrails generally formed parts of all bridges that need to be repaired due to vehicle crashes as well as deterioration over time (Figure 16).

Figure 16. Superstructure repair

3.4. System repair

Restitution project was one of the most difficult works for bridges to construct the completely demolished arch structure again. As the original geometric structure of the belt was difficult to estimate, the characteristics of the destroyed belt should be determined very well, the new one should be made in accordance with the original and projected as a result of the analyzes. At the end of the examination at Orenkit Bridge, the location of the damaged arch was determined and wooden molds were made. Then, from the arch stones side wall and fill materials were placed in the middle and the top structure was built with a single row of cut stones. In the last stage, the bridge railings were completely replaced (Figure 17). As a result of the studies, the belt was replaced by the belt which was destroyed [4].

Figure 17. Repair works at Orenkit Bridge [4]

3.5. Environmental drainage

The elements forming the bridges in places exposed to acid rain or sulphate effect deteriorate prematurely. This caused different stresses in the superstructure and caused damage to the bridges. Therefore, it was

extremely important to prevent the surface and groundwater from having a negative impact on the bridge. For this purpose, a proper drainage system should be built around the bridge to remove water from the environment [4].

3.6. FRP Reinforcing with Rods and Fabric

Energy damping of stone arch bridges exposed to strong dynamic loads caused structural damage and cracks. For this reason, additional elements, FRP (fibrous polymer) rods, which would add ductility to the bridge during the reinforcement and received tensile stresses should be placed. The raw material of FRP fabrics was carbon, glass or aramid based fibers. Most preferred were carbon based fabrics which were very easy to use and practical. These fibers were used to increase the bearing capacity and ductility by placing them on the walls and arches. This method was a solution method applied to keep the parts at risk of disintegration together. However, they were generally not preferred because it disrupted the original structure of the bridge (Figure 18).

Figure 18. FRP strengthening [9]

4. Results

The main factor in the damage of historical stone arched bridges was the flood damages. Flood damage could cause considerable damage to the foot of the bridge, although there was flood splitter in the bridges. Flooding, tree trunks and other drifting materials could cause serious damage to bridges and cause destruction. In addition to flood damages, damages could also occur due to earthquake effects. Great bridge weight increased earthquake impact strength. Depending on the severity of the damage, it could cause partial or complete damage to the bridge. Human-induced damage, such as overloading, changing the slope of the bridge, wars, and lack of proper material, often occurred in local areas of the bridge. The restoration of these damages caused by various reasons locally or general was very important for our cultural heritage. In addition, it was important to have a certain knowledge for repair and strengthening works. Otherwise, the restoration works would not ensure that these structures would survive for many years and this historical wealth would be wasted. It was important to pay attention to the works to be done, the historical structure of the repair and strengthening of the historical tissue was not damaged.

Considering the level reached by today's technology, there were many methods and options for repair. In these applications, it was very important to understand the real behavior of the bridge and arrange the applications according to this behavior. It was also very important that the archive and feasibility studies were carried out meticulously. The date of repair should be done without damaging the tissue and care should be taken to keep the parts reflecting the characteristics of the period. Injection filling of cracks could be applied to locally damaged areas of the bridge without damaging. Bridges exposed to strong dynamic loads also caused structural damage. For this reason, additional elements, FRP reinforcing could be applied locally. Bridges damaged as a result of damages could be repaired partially or completely.

References

[1] Erdal, H. I. (2005). *Inspection and Maintenance Management at Bridges* (Master Thesis, Natural and Applied Sciences, Istanbul University, Turkey).

[2] Yucel, A. and Namli, R. (2007). Investigation of the Effects of Water and Other Factors on Distortion Around Bridge Legs, Eastern Anatolia Region Research.

[3] Bayraktar, A., Altunisik, A. C., Turker, T. and Sevim, B. (2007). The Effect of Finite Element Model Updating on Earthquake Behaviour of Historical Bridges, *Sixth National Conference on Earthquake Engineering*, Proceedings Book, 29-40.

[4] Ural, A., Oruc, S. and Dogangun, A. (2007). Restoration and strengthening of historical arch bridges in the eastern black sea region, Structure World Magazine, 132, 48-53.

[5] Alaboz, M. (2008). *Evaluation of Actual Structural Conditions of Mimar Sinan Bridges in Marmara Region and Kapuagası Bridge Restoration Project (*Master Thesis, Natural and Applied Sciences, Istanbul Technical University, Turkey).

[6] Korkmaz, K. A., Zabin, P., Çarhoğlu, A. I. and Nuhoğlu, A. (2013). Seismic behavior investigation of arc stone bridges: Timisvat bridge case. *Journal of Advanced Technology Sciences*, 2(1), 66-75.

[7] Fırat, F. K. and Eren, A (2015). Investigation of FRP effects on damaged arches in historical masonry structures, *Journal of the Faculty of Engineering and Architecture of Gazi University*, 30(4).

[8] Alpaslan, E., Haciefendioglu, K., Birinci, F. and Kurt, M. (2015). Linked to Local Empowerment in Historical Buildings Local Rigidity Effect of Growth Structure Conduct, *Turkey Earthquake*

Engineering and Seismology Conference Proceedings.

[9] Koc, D. (2015). *Strengthening Stone Arches in Historical Buildings with FRP* (Master Thesis, Natural and Applied Sciences, Aksaray University, Turkey).

[10] Ilerisoy, Z. Y. and Sagir, M. (2016). Factors Deteriorating Historical Bridges and Investigation of Tercan Kotur Bridge in Erzincan, *International Erzincan Symposium*.

[11] Eren, A. (2018). *Repairing of Masonry Arches* Using *FRP in Historical Structures* (Master Thesis, Natural and Applied Sciences, Aksaray University, Turkey).

[12] URL1(2017),https://www.youtube.com/watch?v=pOT8tlCXTjg. (Online Accessed: 05.08.2019).

[13] Resemini, S. (2003). Seismic Vulnerability of Stone Arch Bridges, University of Sudi di Genova.

[14] Ozcan, Z. (2015). Damage Determination at Historic Sangarius Bridge and Strengthening Recommendations, *3rd Bridges Viaducts Symposium.*

[15] Oliveira, D. and Lourenco P. (2004). Repair of stone masonry arch bridges, ARCH'04, CIMNE, Barcelona, 452–458.